CHALMERS
UNIVERSITY OF TECHNOLOGY

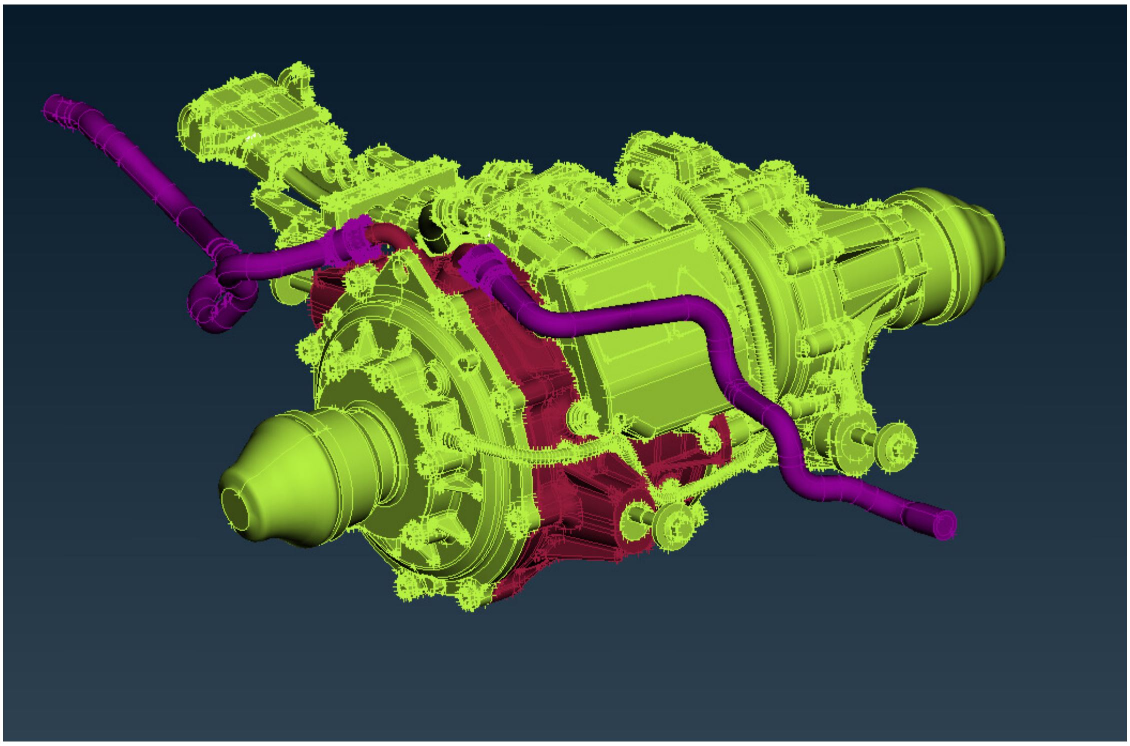

Electric motor internal heat convection modelling and analysis

A Computational Fluid Dynamics Approach

Master's thesis in Applied Mechanics

ANIL KUMAR

Department of Mechanics and Maritime Sciences
CHALMERS UNIVERSITY OF TECHNOLOGY
Gothenburg, Sweden 2018

Electric motor internal heat convection modelling and analysis
ANIL KUMAR

Supervisors:
Randi Franzke, Division of Vehicle Engineering and Autonomous Systems, Chalmers University of Technology
Emma Arfa Grunditz, Division of Electrical Power Engineering, Chalmers University of Technology
Examiner:
Simone Sebben, Head of Division of Vehicle Engineering and Autonomous Systems, Chalmers University of Technology

Master's Thesis 2018:88
Department of Mechanics and Maritime Sciences
Division Vehicle Engineering and Autonomous Systems
Chalmers University of Technology
SE-412 96 Gothenburg
Telephone +46 31 772 1000

Cover: A 3-D representation of the ERAD motor model used for thermal investigation.

Chalmers Reproservice / Department of Mechanics and Maritime Sciences
Gothenburg, Sweden 2018

Electric motor internal heat convection modelling and analysis
Master thesis in Vehicle Engineering and Autonomous Systems
ANIL KUMAR
Department of Mechanics and Maritime Sciences
Chalmers University of Technology

Abstract

An electrified vehicle is a complex thermal environment including a number of components such as electric machines, converters and chargers, which require cooling to function optimally. If the cooling is insufficient, the losses will increase, the performance of the system will be lowered and the life span of the components might be compromised. Currently, the trend to carry out thermal analysis of electric motors is increasing, so as to improve the performance of the machines.

In this thesis, the heat transfer through internal parts of a specific permanent magnet synchronous electric motor (PMSM) is investigated. This type is typically used in hybrid vehicles or fully electric zero emission vehicles.

Varying degrees of geometric complexities was studied. First, a simplified model version of the PMSM was constructed using the pre-processing software ANSA. The numerical analysis of the flow field and heat transfer was done in StarCCM+ which was used as a solver to model and simulate the air flow inside the electric motor. Here, we determine and investigate the dependency of the convective heat transfer coefficients and temperature on the rotational speed of the rotor inside the electric motor.

In order to reduce the computational effort and time, a $1/8^{th}$ section of the simplified motor model was also constructed. The difference in the results obtained from the $1/8^{th}$ motor model case and the full simplified motor case was investigated.

Second, a more complex ERAD (electric rear axle drive) PMSM model was constructed to conduct a conjugate heat transfer analysis. Additional geometric complexities was added compared to the simplified version like the addition of the cooling jackets in the housing part of the electric motor. An investigation of the convectional heat transfer coefficients and temperature distribution on the internal parts of the motor was made with full geometric details with respect to the operating speed of the motor. Furthermore, the coolant flow rate and operating temperatures of the coolant were varied, and investigations were done on how the convectional heat transfer coefficients and temperature of the coolant changes.

Lastly, the temperature values obtained from the ERAD motor were compared with a preliminary reference lumped parameter thermal network (LPTN) model. Here, we noticed a large deviation in the results (higher than +/- 5 °C) near the rotor region which is why further investigation in validation of the heat transfer coefficients are necessary.

It was concluded from the above investigations that the obtained convective heat transfer coefficients are very sensitive to the fluid temperature used. Furthermore, the temperature and the heat transfer coefficients of the internal parts of the electric motor increase with motor speed.

Keywords: Computational fluid Dynamics, Electric motor, PMSM, Conduction, Convection, Heat transfer coefficients, Volvo Cars, ANSA, STAR CCM+

Acknowledgements

This master thesis is conducted as part of the Virtual Hybrid Cooling project (VeHICLe) carried out by Chalmers University of Technology in collaboration with Volvo Car Corporation, Sverige.

I would like to thank the Electric Propulsion Systems (EPS) group (Volvo Cars Corporation) and the Division of Electrical Power Engineering (Chalmers University of Technology) for providing me with the opportunity and resources for my time on this thesis.

I would also like to thank and express my gratitude to all the people that have made this thesis possible, and especially my supervisors Randi and Emma (Chalmers University of Technology) for guiding me in the entire framework of my master thesis and giving me continuous feedback on the method development for the analysis of the electric motor. I would also like to thank Professor Torbjorn Thiringer (Chalmers University of Technology) for his assistance with the lumped parameter thermal network model and also for giving valuable insights on the simulation of the electric motor.

Finally, i would like to thank my examiner Professor Simone Sebben (Chalmers University of Technology) for examining my master thesis work at the Division of Vehicle Engineering and Autonomous Systems at Chalmers University, Gothenburg.

Anil Kumar, Gothenburg, October 2018

Notations

Symbol	Description	SI units
$\dot{Q}_{cond}$	Conductive heat flux density	W
A	Cross sectional Area	$\mathrm{m^2}$
k	Material's thermal conductivity	$\mathrm{Wm^{-1}K^{-1}}$
$\dot{Q}_{conv}$	Convective heat flux density	W
h	convective heat transfer coefficient	$\mathrm{Wm^{-2}K^{-1}}$
T_s	Surface or wall temperature	K
T_{ref}	Reference fluid temperature	K
$\dot{Q}_{rad}$	Radiation heat flux density	W
σ	Stefan Botzmann constant	$\mathrm{Wm^{-2}K^{-4}}$
R_{th}	Thermal resistances	$\mathrm{KW^{-1}}$
C_{th}	Thermal capacitance	$\mathrm{JK^{-1}}$
c_p	Specific heat capacity	$\mathrm{Jkg^{-1}K^{-1}}$
m	mass of the structure	kg
t	thickness of the element	m
ρ	Density of the material	$\mathrm{kgm^{-3}}$
ν	Kinematic viscosity of the fluid	$\mathrm{m^2s^{-1}}$
U_*	Frictional velocity	$\mathrm{ms^{-1}}$
y	Wall distance	m
ΔT_{cool}	Temperature increase in coolant	K
P_{loss}	Heat transfer to the coolant	W
ρ_{cool}	Density for the liquid coolant	$\mathrm{kgm^{-3}}$
$C_{p,cool}$	Specific heat capacity	$\mathrm{Jkg^{-1}K^{-1}}$
$f_{l/min}$	Flow rate of the coolant	$\mathrm{lmin^{-1}}$

Abbreviations

CFD	Computational fluid dynamics
LPTN	Lumped parameter thermal network
PMSM	Permanent magnet synchronous motor
ERAD	Electric rear axle drive
VeHICLe	Virtual hybrid cooling
cond	conduction
conv	convection
rad	radiation
AC	Alternating current
CHT	Conjugate heat transfer
HTC	Heat transfer coefficients

Contents

List of Figures

List of Tables

1 Introduction

This section presents the background for this thesis, its purpose and the delimitations of the project.

1.1 Background

With increasing energy and environmental issues, electric vehicles have taken more and more of people's attention. The driving motor is a key component of electric vehicles. Preferably, it has small volume, high power, high efficiency, high torque, precise control, and is dust and waterproof. However, the driving motor generates high temperatures during operation. [1]. If its thermal limit is exceeded, damages can occur either by the breakdown of stator winding insulation or demagnetization of the magnets, which significantly reduces the reliability and dynamic performance of the motor.

Apart from determining the temperatures at its working conditions, another important aspect of the thesis is to model and simulate the end-windings cooling phenomenon. Typical, in PMSM's (Permanent magnet synchronous motors), the end-windings are the hottest points. An efficient end-winding cooling allows decreasing the temperatures of the windings with better reliability of the motor or, possibly, an increase of the produced steady state torque with the same imposed overtemperature [17]. In electric vehicles, the end-windings are mainly cooled using a liquid WEG (Water Ethylene glycol) coolant. However, the end-windings are also partly cooled by the surrounding internal air inside the motor.
It becomes of utmost importance to predict the right temperatures with a reasonable method to determine this heat transfer due to convection.

A suitable temperature prediction method can thus not only prevent overheating of PMSM in different load situations, but also improve the utilization of the system at normal operating conditions.

Current research on the motor's thermal management generally use equivalent thermal circuit method, lumped parameter thermal network method (LPTN) or finite element method (FEM). Researchers such as R.J.Wang, D.A.Stanton and Y.k.Chin [2, 3] used LPTN and FEM to do the thermal simulation for the driving motor of a vehicle, reporting the motor's temperature field under a specific operating condition.

However, for specifying the convection boundaries used in these methods an analytical/empirical algorithms are used to define them. A more reliable procedure is needed in order to predict the fluid and heat flow in the complex geometry of the electric motor. Thus, the computational fluid dynamics (CFD) technique comes in to picture, which has a better accuracy in predicting the convection phenomenon inside the elcetric motor.

Based on the calculation of losses, this thesis established a more accurate motor thermal simulation model, using CFD for a certain type of water based coolant (ethylene glycol) permanent magnet synchronous motor with a fluid-solid thermal coupling simulation analysis, and got the steady-state three-dimensional temperature field along with the heat transfer coefficients of the motor parts. The validity and accuracy of the simulation results were later compared with a preliminary reference lumped parameter thermal network method.

1.2 Scope

This thesis work comprises the following major steps:

1. Model the internal parts of the electric motor as shown in Figure 1.1 for the Volvo XC90 passenger vehicle using the commercial pre-processor ANSA.
2. Conduct a three dimensional steady state thermal analysis of the electric motor by simulation of the internal air flow using the commercial software Star-CMM+.
3. Investigate the temperature fields and estimate the heat transfer coefficients of the internal parts of the PMSM.
4. Investigation on how the obtained heat transfer coefficients vary with different operating conditions for a PMSM.
5. Finally, to compare the obtained results using a preliminary lumped parameter thermal network modelling techniques to serve as an input for improving the LPTN model for the ERAD.

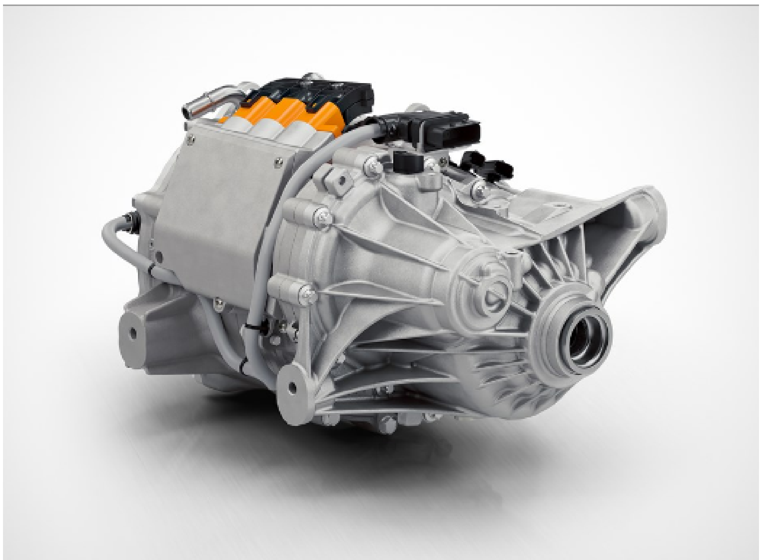

Figure 1.1: Subject motor: electric rear axle drive (ERAD) [4].

1.3 Delimitations

The thesis work has been carried out under the following delimitations:

1. The modelled geometries of the internal parts of the motor do not exactly correlate dimension wise with that of the ERAD motor used in the Volvo XC 90 car, specifically the rotor holes dimensions inside the rotor, the length and width of magnets, geometry of the end winding's due to intellectual property control.
2. Additional parts connected to the motor such as the bearings and the gear box assembly are not included in the analysis.
3. The surface finish for all the parts used in our analysis are considered to be fine.
4. The heat transfer due to radiation in the electric motor is not modelled since it is assumed to account for relatively lower effects compared to conduction and convection which is the highest as per literature for different PMSM's.
5. The simulation results will be examined for consistency from a theoretical perspective. However, a comparison with experimental results is beyond the scope of the present work.

2

Theory

This chapter gives an introduction to the basic modes of heat transfer. A brief discussion on available techniques in thermal modelling of an electric motor and terminologies of different parts in the electric motor is given. It is followed by the topics of computational fluid dynamics modelling relevant to this thesis work.

2.1 Modes of heat transfer

The theory of heat transfer describes the energy transfer that takes place between material bodies as a result of temperature difference. This energy transfer is defined as heat. Heat transfer always occurs from a higher-temperature system to a lower-temperature system. The three modes by which heat can be transferred from one place to another are conduction, convection and radiation. A combination of the above mentioned modes is called as conjugate heat transfer.

2.1.1 Conduction

Thermal conduction is the flow of internal energy from a region of higher temperature to one of lower temperature by the interaction of the adjacent particles (atoms, molecules, ions, electrons, etc.) in the intervening space. Thermal conductivity is the property of a material to conduct heat and evaluated primarily in terms of Fourier's Law for heat conduction which in one dimensional form is given as

$$\dot{Q}_{cond} = -kA\frac{\mathrm{d}T}{\mathrm{d}x} \tag{2.1}$$

where $\dot{Q}_{cond}$ is the heat flow through a cross-sectional area A and k is the thermal conductivity [5].

2.1.2 Convection

The transfer of energy between an object and its environment, due to fluid motion is called convection. The average temperature is a reference for evaluating properties related to convective heat transfer.

Convection can occur usually in the following two ways:

Natural convection: occurs due to density differences and the driving forces are gravity and buoyancy.
Forced convection: occurs by external means such as pumps and fans.

Convective heat transfer is mathematically described by Newton's law of cooling describing the heat transfer between the moving fluid and a solid which is given as

$$\dot{Q}_{conv} = hA(T_s - T_{ref}) \tag{2.2}$$

where $\dot{Q}_{conv}$ is the heat flow through a cross-sectional area A, T_s is the surface or wall temperature and T_{ref} is the reference fluid temperature [5].

2.1.3 Radiation

This mode of heat transfer occurs between any two bodies at different temperatures even without any physical connection or material medium between them. Radiation is a form of electromagnetic emission that is emitted by any body which is at a temperature higher than absolute zero. The emission of an idealized black body can be calculated

$$\dot{Q}_{rad} = \sigma A_s T_s^4 \tag{2.3}$$

and for a non black body this phenomenon is as

$$\dot{Q}_{rad} = \epsilon\sigma A_s T_s^4 \tag{2.4}$$

where A_s and T_s is the area and temperature of the body, $\sigma = 5.67 \times 10^8$ is the Stefan Boltzmann constant and ϵ is the emissivity of the surface that also depends on the temperature of the body and varies within the range $0 < \epsilon < 1$ [5].

2.2 Thermal modelling of electric motor

An electric motor is an electrical machine that converts electrical energy into mechanical energy. Before discussing the thermal phenomenon in an electric motor it is beneficial to look at and understand the classification and construction of an electric motor.
Depending on functionalities and applications there are several types of motors which cannot be discussed here in detail but a glimpse of motors emphasizing their usage in passenger vehicles nowadays is shared in the following sections.

2.2.1 Classification of alternating current(AC) motors

Electric motor's ability to maintain full torque at low speeds are used extensively for vehicle applications. There are two types of AC motors in general classification which are **induction motors** and **PMSM motors** as shown in the Figure 2.1.

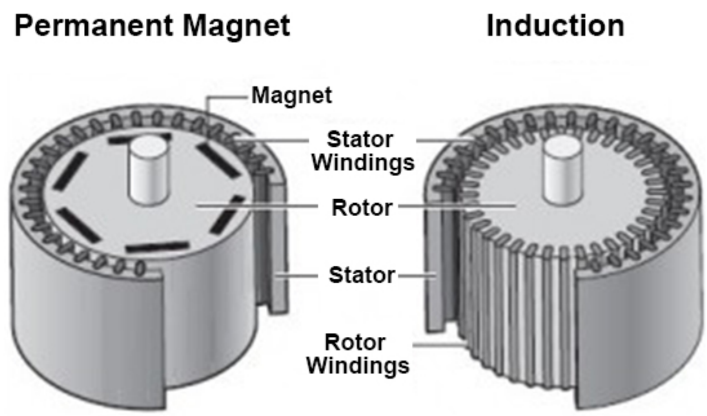

Figure 2.1: Comparison of induction and PMSM [18]

Induction motors relies on electric current that is generated through electromagnetic induction from the magnetic field of the stator windings to turn the rotor whereas the PMSM relies on magnets to turn the rotor [18] and due to this both have a different rotor construction as shown in Figure 2.1 .

However, a permanent magnet motor have higher efficiency and higher power density, compared to an induction motor of the same size. Both PMSM and induction motors make sense for variable-speed drive single-gear transmission as the drive units of the cars but due to higher efficiencies, the PMSM's are the most common type in vehicle applications. [8].

2.2.2 Construction of the ERAD motor

In this section, the different parts that are modelled for our simulations as shown in Figures 2.2, 2.3 and 2.4 are named and their functions are explained briefly to understand the working principles of a PMSM electric motor.

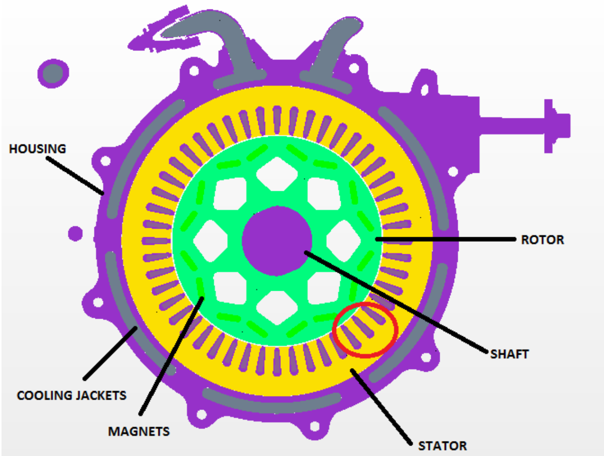

Figure 2.2: Side section view of ERAD

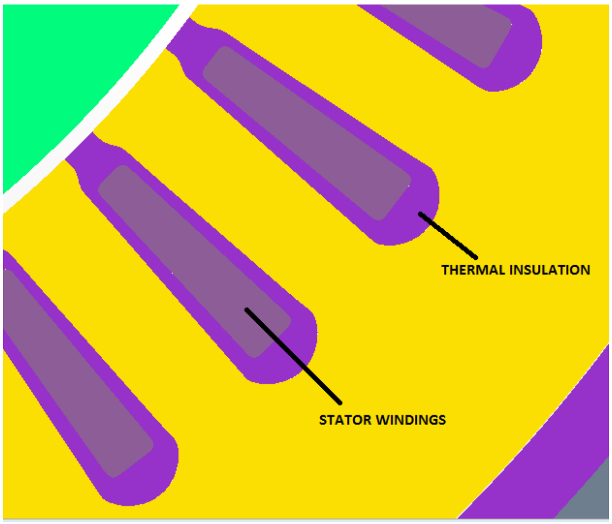

Figure 2.3: Detail view of the windings in ERAD

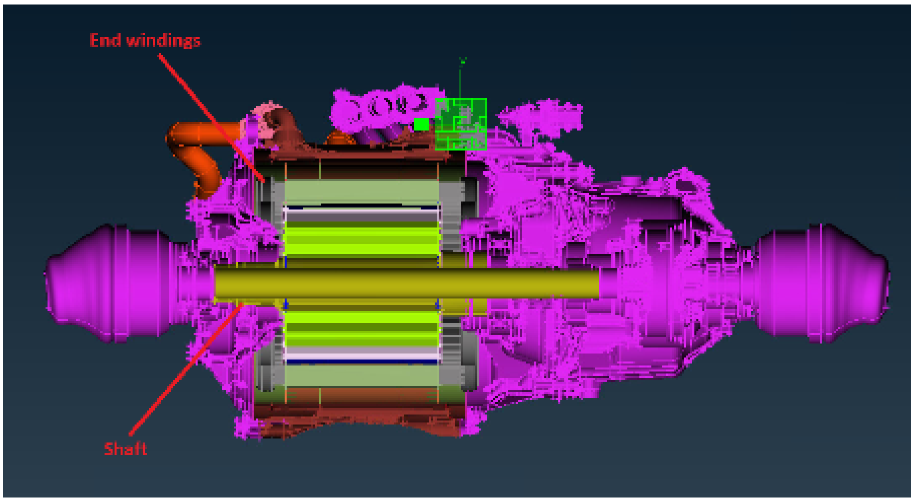

Figure 2.4: Front section view of ERAD

Rotor: In an electric motor, the rotating part is the rotor, which turns the shaft to deliver the mechanical power. The PMSM's rotor has **permanet magnets** in them which produce the necessary magnetic field to interact with the passing currents to generate forces that turn the **shaft**. The rotor core is made up of many thin metal sheets, called laminations. Laminations are used to reduce energy losses that would occur if a solid core was used.

Stator: The stator is the stationary part of the motor's electromagnetic circuit and usually consists of **windings** made of copper materials. The stator core, similar to the rotor core, is made up of laminations.

Windings: Windings are wires that are made out of copper that are laid in coils, usually wrapped to lead magnetic flux through the core so as to form magnetic poles when energized with current. The copper wires in the stator are called the **stator windings** and the windings coming out of the stator ends that are in contact with the air are called the **end windings**.

Air gap: The distance between the rotor and stator is called the air gap. The air gap is needed to avoid friction between rotor and stator. At the same time the magnetizing current increases with the size of the air gap, which reduces the performance. Therefore, the air gap should be minimal. Very small gaps may pose mechanical problems in addition to noise and losses.

Thermal insulation: Around the stator windings in the stator there is usually a thin layer of insulation known as **slot liners** which prevent the entire losses from the windings to transfer to the stator. There are gaps/voids in between the windings which are filled by dipping it in the resins with the process known as **winding impregnation** for improving mechanical stability, electrical insulation, or both.

Housing: The function of the housing is mainly to provide protection for the parts inside of the motor (both from receiving damage and causing damage), and in cases where there is liquid cooling, such as in the ERAD, it also has **cooling jackets** for the liquid coolant to pass through them for efficient cooling of the motor. It is usually made of die casted aluminum and has a direct contact with that of the stator back.

End Caps/Cover: Both endcovers are located at the sides of the motor assembly, it is designed with fins for better thermal heat dissipation, and to ensure low bearing operating temperatures, resulting in extended lubrication intervals and also to reduce the weight without compromising on the mechanical stability.

2.2.3 Heat transfer paths in electric motor

In electric machines, temperature differences and gradients arise due to the inherent internal heat sources that originate from loss mechanisms. The regional temperature differences give rise to transfer of thermal energy, from warmer regions to colder through the three modes conduction, convection and radiation as discussed in the above section [6]. The heat flow paths studied in the thermal modelling of electric motor is as illustrated in Figure 2.5.

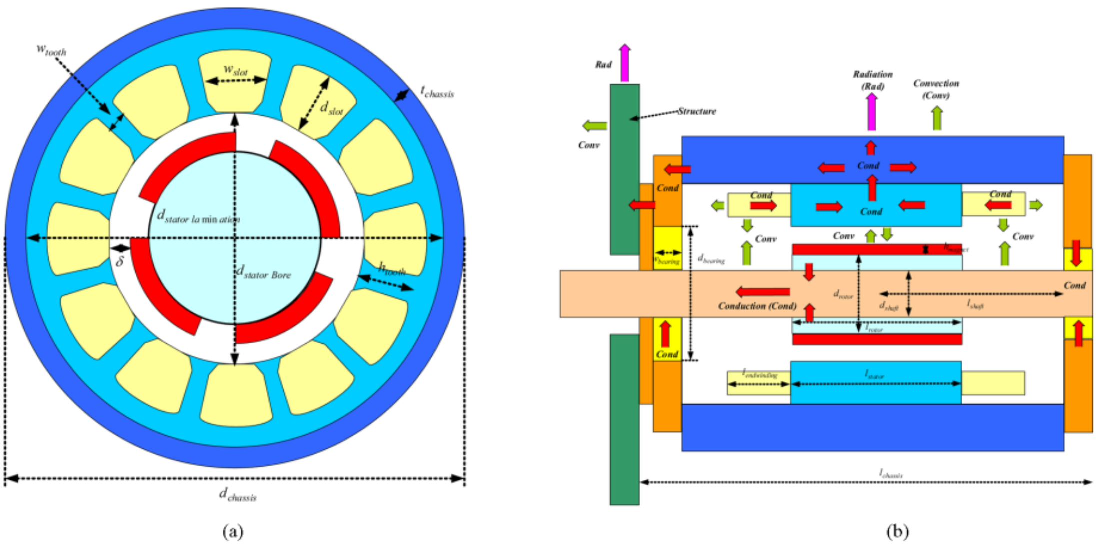

Figure 2.5: a) PMSM motor b) Heat flow diagram [7].

The red arrows (Cond) represent the heat transport due to conduction, the green arrows (Conv) the heat flow due to convection, and the purple (Rad) due to radiation. The (Cond) (Conv) and (Rad) are indicated in Figure 2.5. in the proximity of the arrows [7].

The heat generated inside the motor originates from three main sources; mechanical, electro-magnetic and electrical losses. The mechanical losses include frictional losses generated by the bearings as well as windage losses. The electrical losses include the copper losses in the windings and in the cores, in which there is also electromagnetic hysteresis losses, both referred to as core losses.

It is to be noted from the significant work by researchers David Stanton, Andrea Cavagnino [9], Bin Zhang and Yu Chen [10] that in electric motors the conduction and convection heat transfer phenomenon dominate over the radiation one and therefore the heat flowing through radiation is usually neglected. It is also noted that temperatures of the endwindings inside the electric motor are the highest compared to other parts followed by the stator windings.

2.2.4 Electric motor thermal analysis techniques

There are two commonly used techniques for electric motor thermal analysis [11] that have been developed over the years which are namely:

- **The lumped parametric thermal network**
- **The finite element/volume method such as CFD**

2.2.4.1 Lumped parameter thermal network

In the past decades the method, proposed by Mellor and Turner [12], was a reference method for many researchers working on electric motor thermal problems. Their lumped parameter model is based on subdividing the motor into several parts (also called lumps or elements) that are assumed to have constant temperature and similar thermal behaviour. The amount of energy flowing between adjacent elements depends on mutual temperature difference and interrelated thermal resistance between those elements. The accuracy of such a model mostly depends on the sufficient amount of elements, on correct estimation of the main thermal paths and on realistic assessment of thermal resistance between elements. If the network is correctly defined, it can offer fast and accurate temperature estimates. A typical lumped parameter thermal network model is as shown in Figure 2.6 and is usually 1D in nature. Here, the nodes of interest and thermal resistances that are shown in the Figure 2.6 are obtained from the following empirical relations.
The thermal resistance (R_{th}) for conduction is defined as

$$R_{th} = \frac{t}{Ak} \tag{2.5}$$

where t is the thickness of the element, A is the cross sectional area and k is the material thermal conductivity.

The thermal resistance (R_{th}) for convection is defined as

$$R_{th} = \frac{1}{Ah} \tag{2.6}$$

where h is the convectional heat transfer coefficient.

The stored thermal energy in the different nodes is modeled by thermal capacitance (C_{th}) which is given as

$$C_{th} = mc_p \tag{2.7}$$

where m is the mass of the structure and c_p is the specific heat capacity.

And P denoted in Figure 2.6 are the power losses in the different parts of the PMSM.

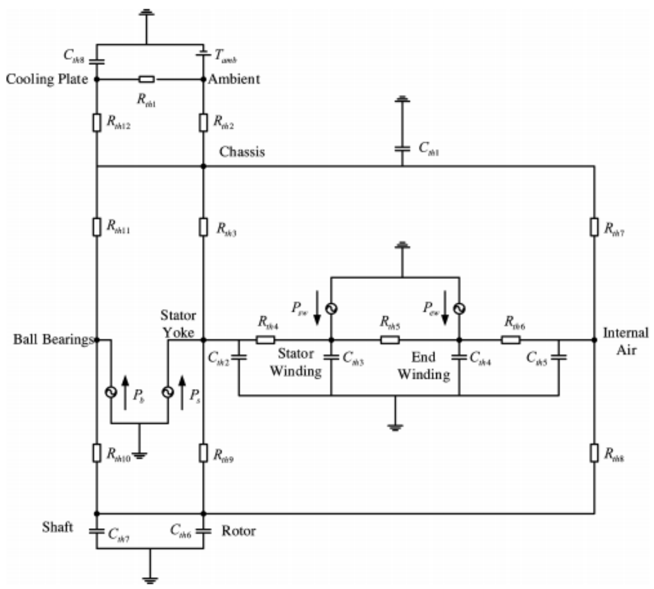

Figure 2.6: Thermal equivalent network representing a PMSM [7].

However, the developer of a network model must invest effort in defining a circuit that accurately models the main heat-transfer paths. In addition, it does not account for any detail air flow model compared to the CFD technique where a turbulence model is incorporated making LPTN less reliable.

2.2.4.2 Computational fluid dynamics

Computational fluid dynamics (CFD) is a numerical tool that can be used to predict fluid flow and heat transfer in complex situations where standard solutions and experimental correlations are not available. It is particularly useful for modelling complex geometries and gives the motor designer the opportunity to predict fluid flows and heat transfer in areas such as around end windings and rotors where little experimental data is available.
It involves solving partial differential equations and in particular the Navier Stokes equation in honor of M. Navier and G. Stokes who independently obtained the equations in the first half of the nineteenth century [13]. The CFD simulations are usually 2D/3D in nature and are often very time consuming. The accuracy of the solution depends on various factors like the geometry and mesh size.

2.3 Introduction to CFD

Computational fluid dynamics (CFD) is a branch of fluid mechanics that uses numerical analysis and generated mesh to solve and analyze problems that involve fluid flows. In thermal analysis of electric motors, CFD is better suited than the conventional LPTN technique, to model parts of a machine as it gives the designer the opportunity to predict air flows and heat transfer coefficients for particular regions. This data can then be used as input for a lumped circuit analysis of the machine as a whole.

2.3.1 Governing equations of fluid flow

The main task in fluid dynamics is to find the velocity field describing the flow in a given domain. To do this, one uses the basic equations of fluid flow, which encodes the familiar laws of mechanics:

- conservation of mass
- conservation of momentum
- conservation of energy

The three basic equations of mass, momentum and energy conservation for an incompressible fluid flow are given in Eqs 2.8, 2.9, 2.10.

$$\frac{\partial u_i}{\partial x_i} = 0 \tag{2.8}$$

$$\frac{\partial u_i}{\partial t} + u_j \frac{\partial u_i}{\partial x_j} = -\frac{1}{\rho}\frac{\partial p}{\partial x_i} + \nu \Delta u_i \tag{2.9}$$

$$\frac{\partial e}{\partial t} + u_j \frac{\partial e}{\partial x_j} = \phi + \frac{1}{\rho}\frac{K \frac{\partial T}{\partial x_j}}{\partial x_j} \tag{2.10}$$

where u_i is the velocity component in the i-th direction, p is the pressure, ρ and ν denote the density and the kinematic viscosity of the fluid respectively. Also Δ is the Laplacian operator, e is the internal energy per unit mass and ϕ is the viscous dissipation per unit mass given as:

$$\frac{\nu}{2}\left(\frac{\partial u_i}{\partial x_j} + \frac{\partial u_j}{\partial x_i}\right)\left(\frac{\partial u_i}{\partial x_j} + \frac{\partial u_j}{\partial x_i}\right) \tag{2.11}$$

In turbulent flows that occurs in most engineering applications, it is too computationally demanding to resolve all turbulent scales. One way to reduce the computational resources needed is averaging. Averaging the flow variables in time, decomposing the instantaneous velocity and pressure into one time averaged (U_i, P_i) and one fluctuating part (u_i', p_i') according to

$$u_i = U_i + u_i' \tag{2.12}$$

$$p_i = P_i + p_i' \tag{2.13}$$

and inserting the result into the governing equations yields the time averaged Navier-Stokes equations, also known as Reynolds Averaged Navier-Stokes (RANS).

The Reynolds averaged Navier Stokes (RANS) equations are given as:

$$\frac{\partial U_i}{\partial x_i} = 0 \tag{2.14}$$

$$U_j \frac{\partial U_i}{\partial x_j} = \frac{\partial[\frac{-P}{\rho}\delta_{ij} + 2\nu \bar{S_{ij}} - \bar{u_i'}\bar{u_j'}]}{\partial x_j} \tag{2.15}$$

where δ_{ij} is the Kronecker delta function and $\bar{S_{ij}}$ is the mean strain tensor which is given as:

$$S_{ij} = \frac{1}{2}\left(\frac{\partial U_i}{\partial x_j} + \frac{\partial U_j}{\partial x_i}\right) \tag{2.16}$$

The terms $\bar{u_i'}\bar{u_j'}$ in Eq 2.15 is referred to as the Reynolds stresses and these terms are to be modelled in order to solve the RANS equation. In other words, it is also known as the closure problem since it introduces many velocity unknowns and therefore needs more equations.

2.3.2 Near wall modelling

Turbulent flows are significantly affected by the presence of walls. Obviously, the mean velocity field is affected through the no-slip condition that has to be satisfied at the wall [14]. Very close to the wall, viscous damping reduces the tangential velocity fluctuations, while kinematic blocking reduces the normal fluctuations. Toward the outer part of the near-wall region, however, the turbulence is rapidly augmented by the production of turbulence kinetic energy due to the large gradients in mean velocity.
The wall y^+ is the non-dimensional wall distance for a wall-bounded flow and can be defined in the following way:

$$y^+ = \frac{U_* y}{\nu} \tag{2.17}$$

where U_* is the frictional velocity, y is the wall distance and ν is the kinematic viscosity.

Numerous experiments have shown that the viscous-affected region can be largely made up of three layers with their corresponding wall y^+ as shown in the Figure 2.7.

- Viscous sublayer ($y^+ < 5$)
- Buffer layer ($5 < y^+ < 30$)
- Fully turbulent or log-law region ($30 < y^+ < 300$)

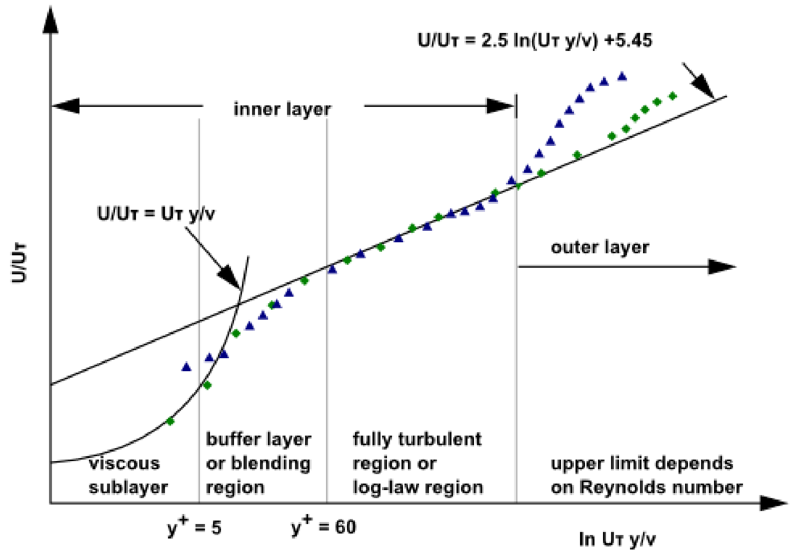

Figure 2.7: Subdivisions of the Near-Wall Region [14].

Traditionally, there are two approaches to modeling the near-wall region. In one approach, the viscosity-affected inner region (viscous sublayer and buffer layer) is not resolved. Instead, semi-empirical formulas called **wall functions** are used to bridge the viscosity-affected region between the wall and the fully-turbulent region. The use of wall functions obviates the need to modify the turbulence models to account for the presence of the wall.
In another approach, the turbulence models are modified to enable the viscosity-affected region to be resolved with a mesh all the way to the wall, including the viscous sublayer. This is termed the **near-wall modeling approach**. These two approaches are depicted schematically in Figure 2.8.

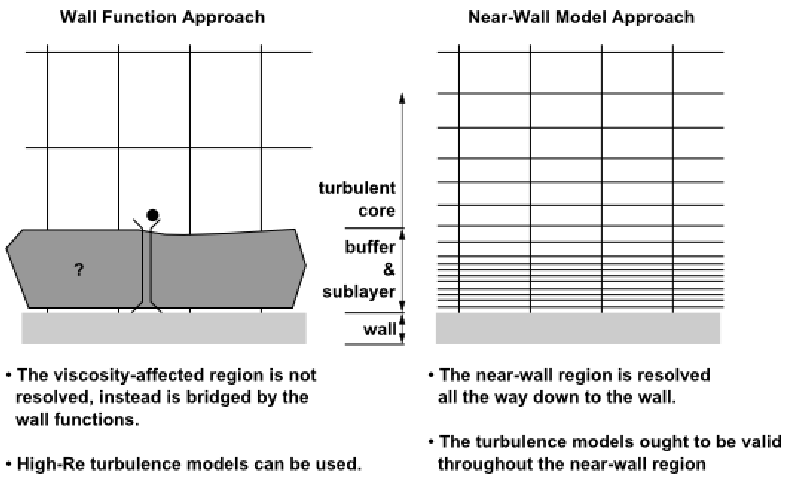

Figure 2.8: Near-Wall Treatments [14].

In StarCCM+, these approaches are available when defining the continua of the turbulent fluid namely:

- The high-y^+ wall treatment implies the wall function type approach in which it is assumed that the near-wall cell lies within the logarithmic region of the boundary layer.
- The low-y^+ wall treatment is suitable only for low Reynolds number turbulence models in which it is assumed that the viscous sub-layer is properly resolved.
- The all-y^+ wall treatment is a hybrid treatment that attempts to emulate the high-wall treatment for coarse meshes and the low-y^+ wall treatment for fine meshes. It is also formulated with the desirable characteristic of producing reasonable answers for meshes of intermediate resolution.

2.3.3 Turbulence modelling

There are different turbulence models available to close the RANS equation system, however one has to carefully consider the advantages and disadvantages of each one to select an appropriate model based on the simulation necessity to accurately predict flows.

Realizable k-ϵ model:

In this model, the approximation for the Reynolds stress is based on the Boussinesq assumption, i.e.

$$-\rho\bar{u_i'}\bar{u_j'} = 2\mu_t S_{ij} - \frac{2}{3}k\delta_{ij} \tag{2.18}$$

where k is the turbulent kinetic energy and ϵ is the turbulent dissipation and μ_t is given as $\mu_t = \rho C_\mu \frac{k^2}{\epsilon}$, One of its major shortcomings is the fact that the equation for ϵ does not go to zero at the wall. Therefore, additional highly non-linear damping functions are needed to be added to low-Reynolds formulations meaning entering the viscous sublayer to be able to integrate through the laminar sublayer ($y^+ < 5$).

Wilcox k-ω model:

In Wilcox's k-ω model in contrast to the realizable k-ϵ model, it could be shown by looking at the wall boundary conditions that the rate of dissipation ω equation takes an “elliptic” near wall behavior. This means that it has an inherent nature of being able to “communicate” with the wall and has a Dirchlet boundary conditions. The term “elliptic” is used with respect to a concept introduced to the ϵ-equation in the k-ϵ turbulence model in order to avoid the need for damping functions for the viscous/laminar sublayer. The concept of elliptic relaxation can be easily shown to be an inherent feature of the k-ω turbulence model only by inspecting the ω-equation in the near wall region when combined with the specified ω values at the wall :

$$\mu\frac{\partial^2\omega}{\partial x_j^2} = \beta\rho\omega^2 \tag{2.19}$$

The implication of such behavior is the straightforward integration through the laminar sublayer without additional numerically destabilizing damping functions or two more transport equations which shall generally cause stabilization issues due to reciprocity between the variables. However, one of the shortcomings of Wilcox k-ω is that the model depends strongly on free-stream values of ω that are specified outside the shear layer.

SST k-ω model:

To alleviate both shortcomings of each method: the near wall behavior of realizable k-ϵ and the ambiguity to freestream values of ω of that of Wilcox k-ω in one formulation, Menter decided to blend them continuously. The Wilcox k-ω is then applied in the near-wall region and the realizable k-ϵ is reformulated in a k-ω form and applied towards the end of the boundary layer, thereby getting the best out of both. Menter did this by using a blending function to implement the what is known as Bradshaw's assumption, that the shear-stress in the boundary layer is proportional to the turbulent kinetic energy results in one of the most reliable RANS turbulence models which is Menter's k-ω SST. The SST model accounts for cross-diffusion which better marries the k-ϵ and k-ω models. Using a blended function based on wall distance, engineers can include cross-diffusion when away from the wall but not near it. In other words, using the wall distance as a switch, SST works like k-ϵ in the far field and k-ω near the target geometry making it a popular choice among engineers. The main shortcomings of this model is that the blending function crossover location is arbitrary and could obscure some critical feature of the turbulence. Moreover, it also requires limiters to improve the prediction of stagnant regions of the flow. Additionally, it has issues predicting turbulence levels and complex internal flows and it doesn't take buoyancy into account.

Reynolds stress model:

Reynolds stress model (RSM) is the most complete physical representation of turbulent flows. It is able to capture complex strains like swirling flows and secondary flows. For swirling flows, such as cyclones, RSM is the only accurate closure model. This model is based on the six equations that represent turbulent stresses. However, this model is highly computationally expensive since it solves for six additional equations and one of the most difficult turbulence model to use in any simulations since the convergence of the solutions is not easy to attain.

The Reynolds stress model involves calculation of the individual Reynolds stresses for the closure problem that are calculated using differential transport equations. The exact transport equations for the transport of the Reynolds stresses $\bar{u_i'}\bar{u_j'}$ may be written as:

$$\frac{\partial(\rho\bar{u}_i'\bar{u}_j')}{\partial t}+\frac{\partial(\rho u_k\bar{u}_i'\bar{u}_j')}{\partial x_k}=-\frac{\partial[\rho\bar{u}_i'\bar{u}_j'\bar{u}_k'+\bar{p}'(\bar{\partial}_{kj}\bar{u}_i'+\bar{\partial}_{ik}\bar{u}_j')]}{\partial x_k}$$
$$+\frac{\partial[\mu\frac{\partial(\bar{u}_i'\bar{u}_j')}{\partial x_k}]}{\partial x_k}-\rho(\bar{u}_i'\bar{u}_k'\frac{\partial u_j}{\partial x_k}+\bar{u}_j'\bar{u}_k'\frac{\partial u_i}{\partial x_k})$$
$$+\bar{p}'(\frac{\bar{\partial}u_i}{\partial x_j}+\frac{\bar{\partial}u_j}{\partial x_i})-2\mu\frac{\bar{\partial}u_i'}{\partial x_k}\frac{\bar{\partial}u_j'}{\partial x_k}$$
$$-2\rho\Omega_k(\bar{u}_j'\bar{u}_m'\epsilon_{ikm}+\bar{u}_i'\bar{u}_m'\epsilon_{jkm}) \tag{2.20}$$

or Local Time Derivate + C_{ij} = $D_{T,ij}$+$D_{L,ij}$+ P_{ij} +ϕ_{ij} -ϵ_{ij} + F_{ij}

where C_{ij} is the Convection-Term, $D_{T,ij}$ equals the Turbulent Diffusion, $D_{L,ij}$ stands for the Molecular Diffusion, P_{ij} is the term for Stress Production, ϕ_{ij} is for the Pressure Strain, ϵ_{ij} stands for the Dissipation and F_{ij} is the Production by System Rotation.

2.3.4 Convective heat transfer coefficients

The convective heat transfer coefficient in thermodynamics and in mechanics is the proportionality constant between the heat flux and the thermodynamic driving force for the flow of heat, i.e. the temperature difference ΔT. It is based on Newton's law of cooling which is given as:

$$h=\frac{\dot{Q}_{wall}}{T_w-T_{fluid}} \tag{2.21}$$

$\dot{Q}_{wall}$ = Heat flux from wall (W/m^2),
T$_w$ = Wall temperature (K),
h = Heat transfer coefficient (W/m^2K)

In StarCCM+, when the energy equation (2.10) is solved, there are three types of heat transfer coefficients available:

Heat transfer coefficient: uses the fluid temperature specified by the user which is usually the inlet temperature of the fluid or bulk temperature for internal flows and free stream temperature for external flows. The drawback of this heat transfer coefficient is that it does not account for local variations in fluid temperature.

Local heat transfer coefficient: uses the near wall cell fluid temperature and this temperature is found on the field function *Local Heat Transfer Reference Temperature*. The local HTC is not to be used when using near wall modelling techniques since the associated reference temperature is very similar to the wall temperature and loses its common interpretation, possibly reaching extremely high values.

Specified y^+ heat transfer coefficient: uses the fluid temperature determined at a user specified y^+ away from the wall and this temperature is found on the Field Function *Specified y^+ Heat Transfer Reference Temperature*. The specified y^+ HTC accommodates local fluid temperature variation effects and also eliminates the near wall mesh sensitivity which is seen in the earlier HTC's and therefore is recommended as a best practice.

Regardless of the method chosen to determine HTC, it is important to note that all the heat transfer coefficients are dependent on the right determination of the fluid temperature (T_{fluid}) that is used to calculate these values.

2.3.5 Moving reference frame

A Moving Reference Frame (MRF) is a relatively simple and efficient steady-state modeling technique to simulate rotating machinery without actually rotating the mesh in the model.
An MRF assumes that an assigned volume has a constant speed of rotation and the non-wall boundaries are surfaces of revolution.

Consider a coordinate system that is translating with a linear velocity $\overrightarrow{v_t}$ and rotating with angular velocity $\overrightarrow{\omega}$ relative to a stationary (inertial) reference frame, as illustrated in Figure 2.9.

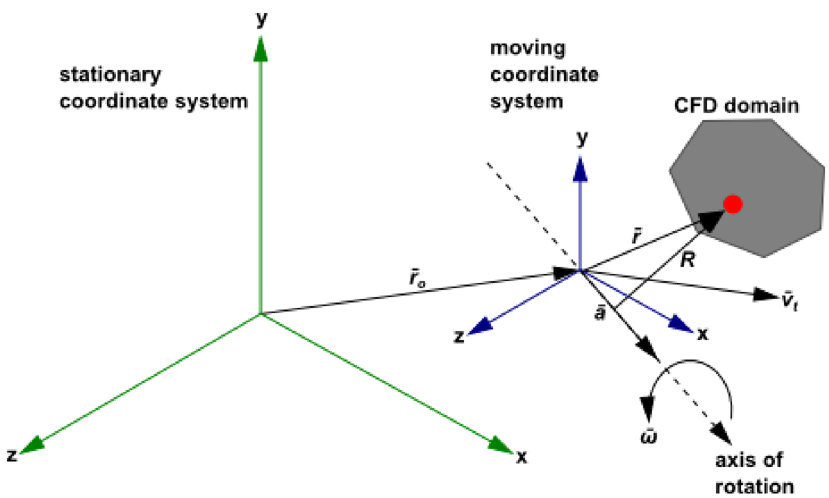

Figure 2.9: Stationary and moving reference frames [14]

The origin of the moving system is located by a position vector $\overrightarrow{r_o}$. The axis of rotation is defined by a unit direction vector $\widehat{a}$ such that

$$\overrightarrow{\omega} = \omega \widehat{a} \tag{2.22}$$

The computational domain for the CFD problem is defined with respect to the moving frame such that an arbitrary point in the CFD domain is located by a position vector $\overrightarrow{r}$ from the origin of the moving frame.

The fluid velocities can be transformed from the stationary frame to the moving frame using the following relation:

$$\overrightarrow{v_r} = \overrightarrow{v} - \overrightarrow{u_r} \tag{2.23}$$

$$\overrightarrow{u_r} = \overrightarrow{v_t} + \omega \times \overrightarrow{r} \tag{2.24}$$

In the above equations, $\overrightarrow{v_r}$ is the relative velocity (the velocity viewed from the moving frame), $\overrightarrow{v}$ is the absolute velocity (the velocity viewed from the stationary frame), $\overrightarrow{u_r}$ is the velocity of the moving frame relative to the inertial reference frame, $\overrightarrow{v_t}$ is the translational frame velocity, $\overrightarrow{\omega}$ and is the angular velocity [14].

A typical example on how the MRF is modelled in a CFD domain for a mixing tank with a single impeller is as shown in the Figure 2.10.

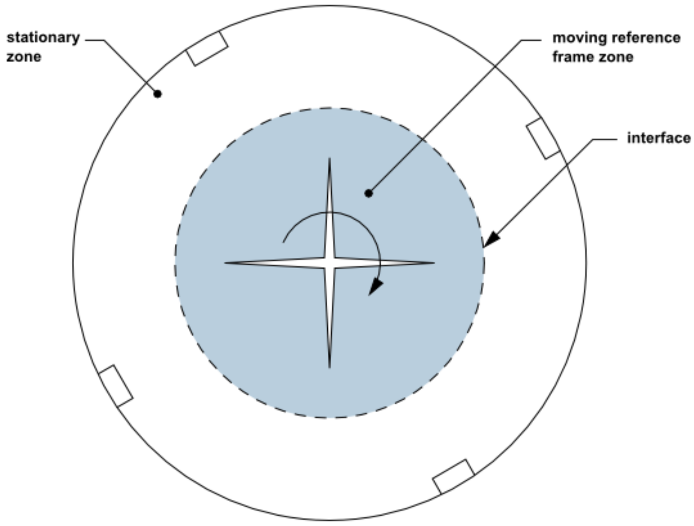

Figure 2.10: Geometry with one rotating impeller [14]

We can define a moving reference frame that encompasses the impeller and the flow surrounding it, and use a stationary frame for the flow outside the impeller region. The dashes denote the interface between the two reference frames. Steady-state flow conditions are assumed at the interface between the two reference frames. That is, the velocity at the interface must be the same (in absolute terms) for each reference frame and the mesh does not move.

3
Methodology

In this chapter, the procedure undertaken to complete the aim of the thesis will be discussed in detail. Altogether, two versions of the electric motor were created: a **simplified version** where this model was analysed only for convection and a **full scale ERAD model** on which a conjugate heat transfer analysis (conduction and convection) was done. It is important to note that the geometry created for the two versions does not have a complete similarity in terms of dimension as the models were updated after the first part of this work to accurately depict the internal parts of the ERAD motor.
We will here begin with a general CFD workflow employed on the two models as shown in Figure 3.1.

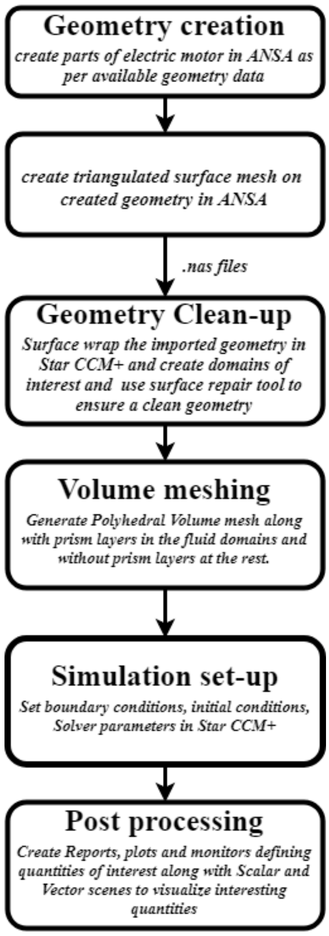

Figure 3.1: Schematic overview of workflow

3.1 Geometry creation

In this thesis, ANSA 18.1.0 from BETA CAE Systems S.A. was used to create surface models for the internal parts of the electric motor for both **simplified** as well as **full scale ERAD model** of the electric motor. However, for the full scale ERAD model the exterior frame along with cooling jackets were obtained from Volvo Cars. Additionally, $1/8^{th}$ section of the motor model was extracted from the simplified case to solve for convection due to geometrical symmetry of the motor model. This model was analysed only for one specific torque and speed of the electric machine to note key differences with respect to the simplified case and make valid discussions on them which will be explained in the results section later on.

Simplified motor model: For this case, there is no external coolant flow, i.e. a very simple housing without cooling jackets was modelled. Furthermore, this model was analysed only for convection due to internal air and therefore the surfaces in contact with the air domain needed to be included. The surfaces of interest were from the rotor, stator, end windings, end caps, the magnets, the housing and the shaft as shown in Figure 3.2. The geometry of the end windings were simplified to a squiril cage construction in order to avoid the modeling of seperate coils. Furthermore, in order to use the MRF model, MRF zones had to be created in accordance with the outlines stated in Section 2.3.5. The MRF zones could not be extended as desired due to the thin limited space around the airgap region in the radial direction of the rotor.

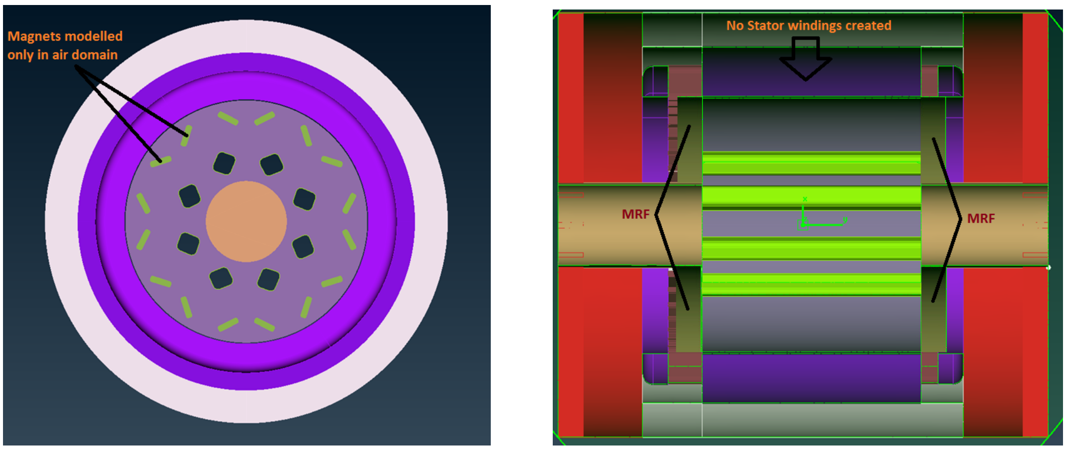

(a) Side view without Endcaps. **(b)** Front sectional view.

Figure 3.2: Geometry of simplified motor model.

$1/8^{th}$ section of simplified motor model: For this case, $1/8^{th}$ section of the simplified motor geometry was extracted and a special attention was given to model the symmetry walls as shown in Figure 3.3. These symmetry walls will act as periodic interfaces when running the simulations on the model. An overview of the parts modelled in the $1/8^{th}$ section of the motor is as shown in Figure 3.3

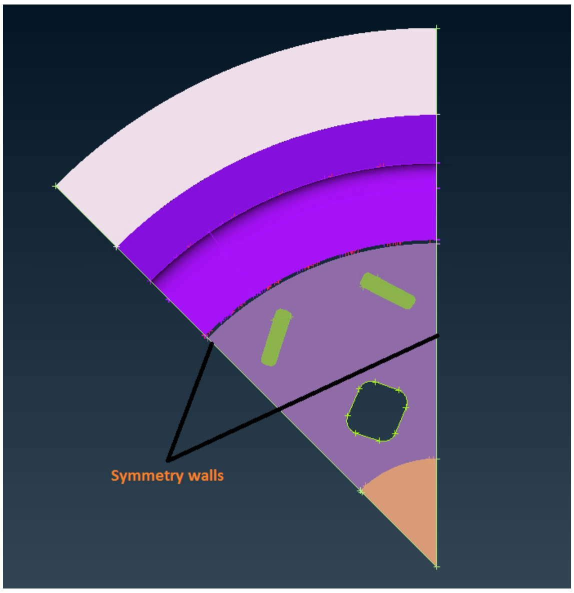

(a) Side view without Endcaps.

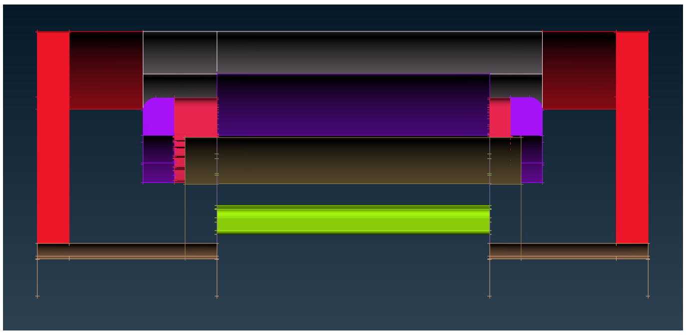

(b) Front sectional view without symmetry walls.

Figure 3.3: Geometry of $1/8^{\text{th}}$ section of simplified motor model.

Full scale ERAD motor model: For this case, the coolant flow was added to the motor model, i.e. housing with the cooling jackets for the coolant to flow was modelled. Further, this model was analysed for conduction of solids as well as convection. The solid parts modelled here are as in Table 3.1 which are pictorially shown in Figure 3.4.
Additionally in this model, thermal insulation was added between the stator windings and the stator as mentioned in the section 2.2.2. Here, the slot liners and the winding impregnation around the copper coils are modelled effectively by considering 45.45% of the total stator slot area to the windings and the rest for thermal insulation.
To model the rotation of the rotor, the MRF technique was chosen and modelled similarly as in the **simplified motor model** case.

Table 3.1: Full scale ERAD model motor parts

Rotor	Stator	End windings
Magnets	Housing with cooling jackets	External frame with end covers
Shaft	Stator windings	Winding thermal insulation

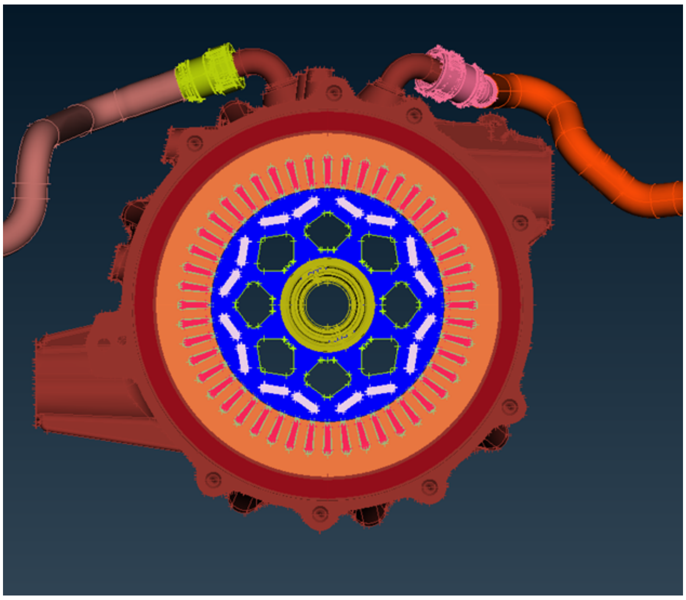

(a) Side view without External frame.

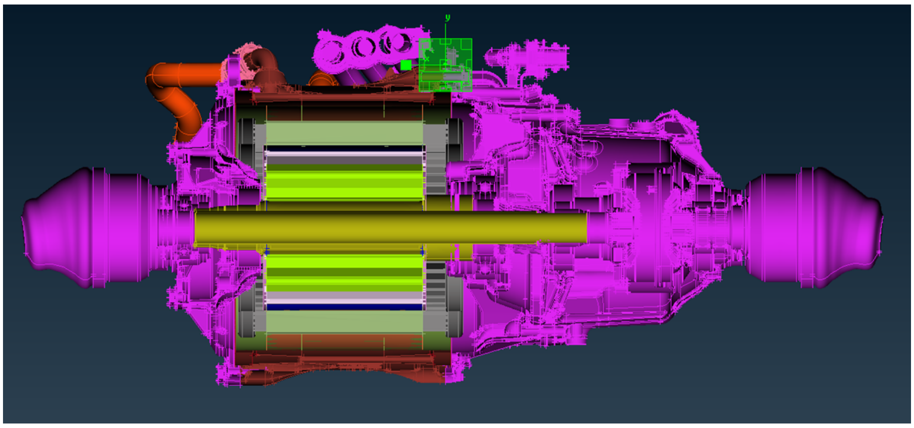

(b) Front sectional view.

Figure 3.4: Geometry of full scale motor model.

Finally, the ANSA file was meshed using STL[1] algorithm to export these models in the ".nas" format for the the Star CCM+ solver to read these files.

[1]The STL algorithm should not be confused with the stl-file format. The algorithm creates a surface triangulation without any restraints on the surface mesh quality, while the file format is a standard on how to store surface triangulation's in files.

3.2 Surface wrapping

The ".nas" files from ANSA were imported to Star CCM+ 13.02 from Siemen's PLM for further procedures. Initially, after the parts were created from the import files a surface wrapping operation was created for all of them, because the initial raw mesh imported from ANSA consists of multiple intersecting surfaces and gaps. Hence, the generation of a well-resolved, water tight surface mesh is required as a first step to avoid numerical problems later on. Additionally, different regions like the rotational region, air region and coolant region were easily obtained from these operations as shown in Figures 3.5, 3.6 and 3.7 for the **simplified case** and for the **full scale ERAD model case**.
When using the surface wrapper operation, sometimes there might be issues of "webbing" near places where there is a small distance between different parts for example near the air gap between rotor and stator which causes overlap of meshes between these regions. To overcome this, we use contact preventions between these parts.

Imprinting parts: Imprinting of the parts after surface wrapper operation is done to create conformal interfaces between regions. In this operation, the coincident faces are merged from different regions resulting in shared common surface between two regions. It also creates so called **weak in place contacts** automatically which are later used to create conformal interfaces manually after the meshing operation is done. A total of 15 interfaces were created for the full scale ERAD model case allowing solid-solid, solid-fluid and fluid-fluid interactions between different regions.

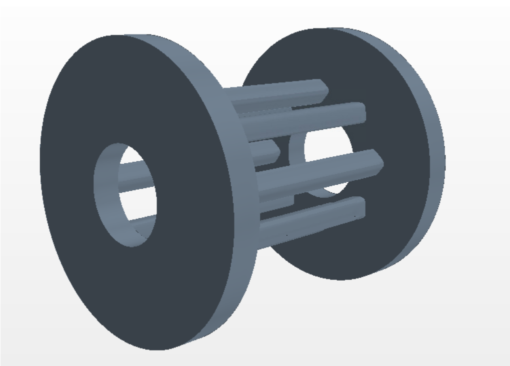

(a) Rotational region for Simplified motor.

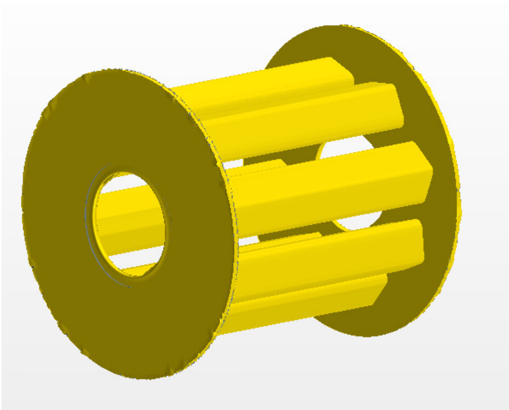

(b) Rotational region for full scale motor.

Figure 3.5: Rotational region.

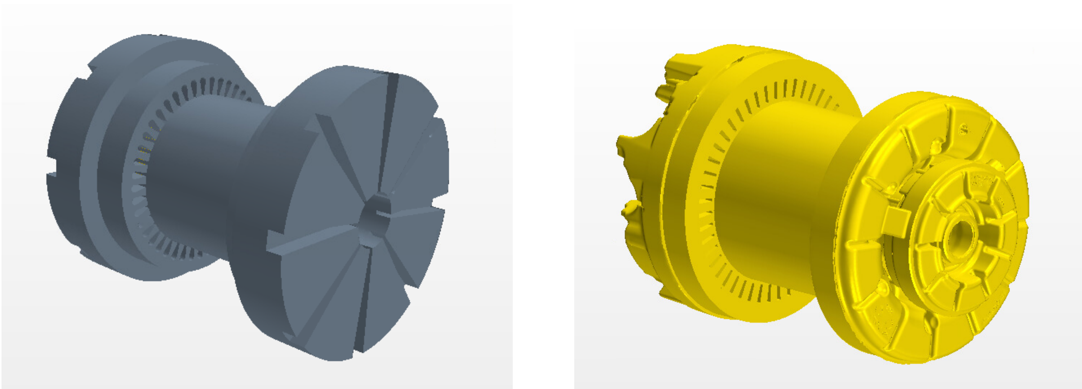

(a) Air region for Simplified motor.

(b) Air region for full scale motor.

Figure 3.6: Air region.

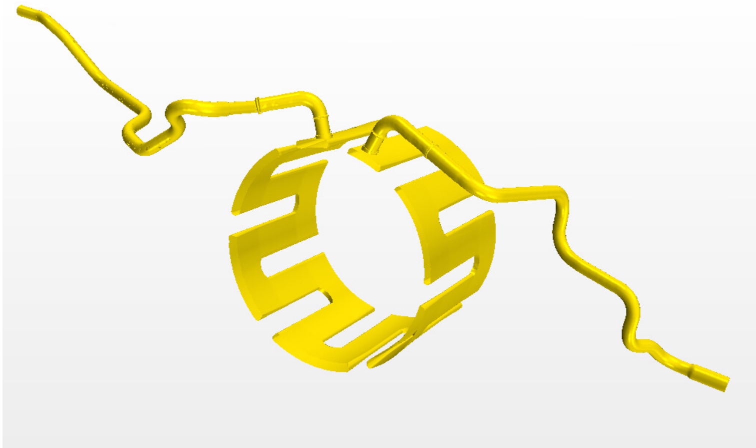

Figure 3.7: Coolant region.

3.3 Volume meshing

Polyhedral meshes were used along with different other settings as shown in Table 3.2. The reason for using the polyhedral meshes is that it creates less number of cells compared to other available meshes and they are inherently widely used for conjugate heat transfer simulations due to their major advantage that it has many neighbors (typically of order 10), so gradients can be much better approximated using linear shape functions and the information from nearest neighbors only, than in the case with other cells [15].

Table 3.2: Models selected for Volume meshing

Solids	**Fluids**
Surface Remesher	Surface Remesher
Automatic Surface Repair	Automatic Surface Repair
Polyhedral Mesher	Polyhedral Mesher
	Prism layer Mesher

Surface remesher: The surface remesher along with the *Automatic surface repair* is used to retriangulate the created surface mesh from the surface wrapper to a better overall quality and optimize the surface mesh for the generation of the volume meshes. Even though they are coupled with the polyhedral meshers, they are performed first as seperate operations when the meshing process is executed.

Prism layer mesher: In order to capture or resolve the strong transverse gradients of the solution (like velocity and temperature etc) within the boundary layer, we generally prefer the prism layers in our polyhedral mesh near the wall. They allow for suitably flow aligned high aspect ratio cells (without any excessive stream wise resolution), thus trying to capture the boundary layer with less numerical diffusion. It is important to note that for the solid meshes we do not use prism layers since there is no boundary layer phenomenon occurring within the solids. A list of values used to create volume mesh is specified in the Table 3.3

Table 3.3: Element sizes for meshes.

Default Base size	2 mm
Target size	100% relative to base
Minimum surface size	75% relative to base
Prism layer total thickness	50% relative to base
Growth Factor	1.3
Number of Prism layers	7

A total final volume generated for the simplified motor which has around 3 million cells and for the full scale model around 75 million cells are shown in the Figures 3.8 and 3.9.

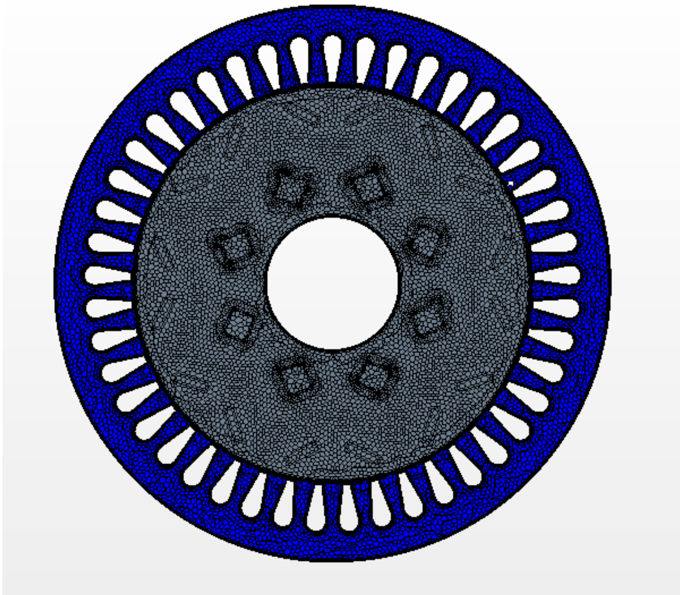

(a) Side sectional view of generated volume mesh.

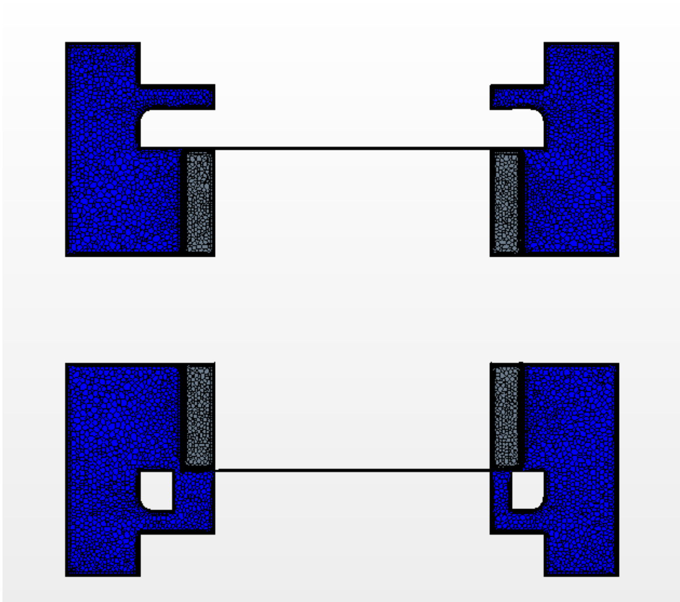

(b) Front sectional view of generated volume mesh.

Figure 3.8: Computational grid for simplified motor.

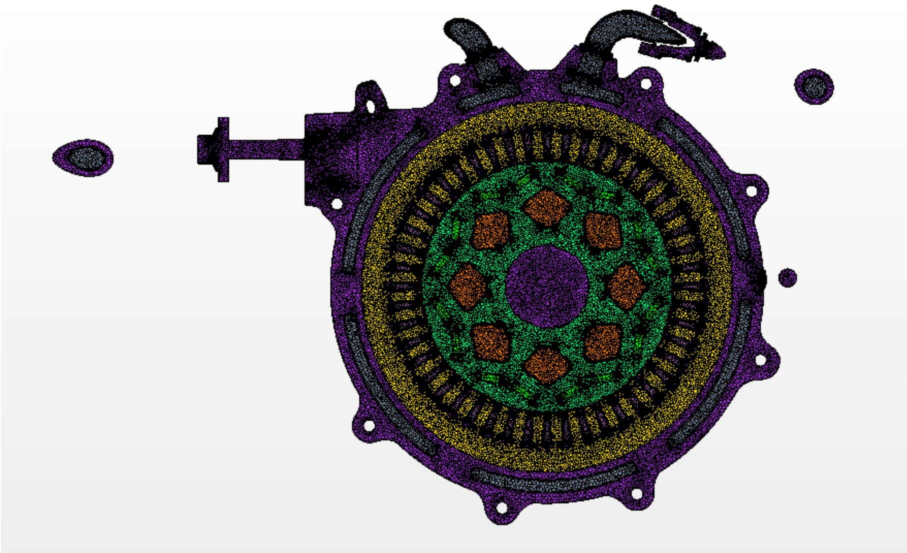

(a) Side sectional view of generated volume mesh.

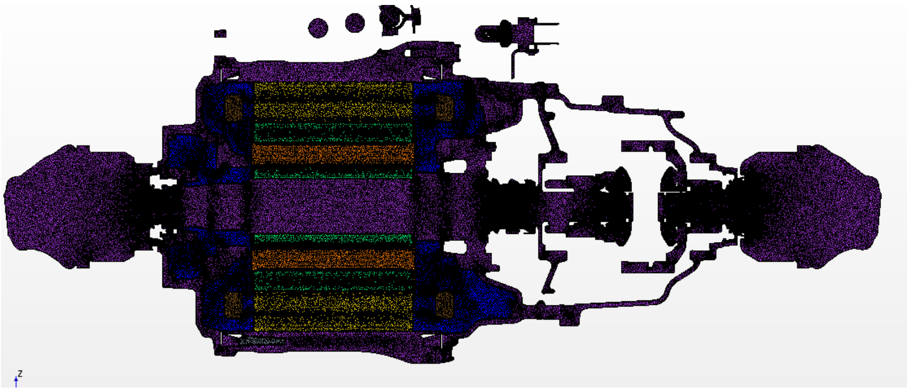

(b) Front sectional view of generated volume mesh.

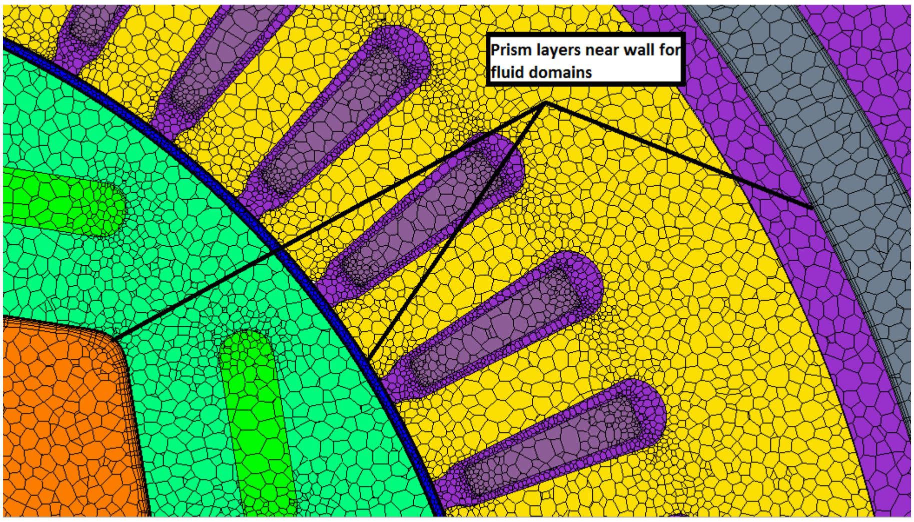

(c) Prism layers near wall for fluid domains.

Figure 3.9: Computational grid for full scale motor.

3.4 Boundary conditions

The thermal boundary conditions are assigned to different parts of the motor.
For the **simplified case**, which only considers convection, the losses were assigned on the boundary surfaces for different parts and their numerical values are as shown in Table 3.4. Here, the numerical values were approximated to a certain percentage to assign on the surfaces of the individuals parts from the total loss maps as shown in Appendix A.1. The loss data used for simplified case analysis were estimated from a different motor (Highway II V-shaped reference motor) that was studied in a PhD thesis [6].
The losses for the simplified case were selected for three different operating points are as shown in the Table 3.4

Table 3.4: Thermal boundary conditions for Simplified motor

Torque (Nm)	Rotation (RPM)	Stator (W)	End Windings (W)	Rotor (W)	Magnets (W)
100	4000	50	100	2	0.2
100	6000	90	160	3	0.8
80	12000	110	190	10	2
	Estimated losses (%)	10%	25%	10%	33%

For the **full scale ERAD motor model**, we were doing a conjugate heat transfer analysis where volumetric heat losses were added to different solid parts. Their numerical values are as shown in the Table 3.5. The losses of the ERAD motor model were obtained from electromagnetic finite element simulations in ANSYS Maxwell, and used as input for the boundary conditions. The numerical values assigned for the different regions in the simulation model were obtained from the loss maps of the ERAD motor as shown in Appendix A.2. The losses for the full scale motor model were selected for four different operating points are as shown in the Table 3.5.

Table 3.5: Thermal boundary conditions for ERAD motor

Torque (Nm)	Rotation (RPM)	Stator (W)	Stator windings (W)	End Windings (W)	Rotor (W)	Magnets (W)
100	1000	69.77	596.904	657.096	1.209	0.001
100	4000	366.8	596.904	657.096	9.504	0.02
100	8000	733.3	1125.3	1238.7	28.12	0.20
80	12000	1281.1	1436.1	1580.9	60.74	0.42

For the CFD simulations, the losses for the stator core are the sum of losses in the teeth and yoke from the loss maps of ERAD. The total winding losses from the loss maps were divided so that 52.4% of the total winding losses are in end windings and 47.6% in the stator windings. Here, it is important to note that the stator windings only include the part of the windings that passes through the stator core.

The boundary conditions for the coolant used which is ethylene glycol water mixture (52-48% in volume), has a mass flow inlet of 0.07 kg/s with the inlet temperature of 313.15 K with fluid material data as shown in Table 3.8.

3.5 Physics set-up

A CFD simulation requires that we configure physics models and solver values based on our knowledge of fluid application. In this work, three different continua or physics models were employed for the simulations as shown in Table 3.6

Table 3.6: Physics models for simulations

Air continua	**Coolant continua**	**Solids continua**
All Y+ wall treatment	Laminar	Gradients
SST(Menter) k-omega	Coupled energy	Coupled solid energy
k-omega turbulence	Coupled flow	Constant density
Exact wall distance	Cell quality remediation	Multi-part solid
Reynolds-Averaged-Navier-Stokes	Constant density	Multi-component solid
Turbulent	Gradients	Cell quality remediation
Coupled energy	Liquid	Three dimensional
Coupled flow	Three dimensional	Steady state
Cell quality remediation	Steady state	
Ideal gas		
Gas		
Gradients		
Three dimensional		
Steady state		

The above mentioned air continua settings are mainly the same for the simplified motor case as well as for the complete ERAD model. Since for the simplified case, we did not solve for conduction of solids and coolant flow, there was no coolant and solid continua. Also in the air continua for the simplified case, elliptic binding Reynolds stress models were used instead of the k-ω turbulence model to ease convergence of the simulations.

The *cell quality remediation* model in StarCCM+, identifies elements of poor quality in the mesh and modifies the way the gradients are computed in the vicinity of those cells, improving the robustness of the simulation in assisting convergence while trying to minimize any negative effect on the accuracy.

The coupled solver formulations were used in this approach in comparison to the segregated solvers. As in the segregated solver formulations the continuity, momentum, and energy equations are solved sequentially (i.e., segregated from one another), while the coupled solver solves them simultaneously (i.e., coupled together). The coupled scheme obtains a robust and efficient single phase implementation for steady-state flows, with superior performance compared to the segregated solution schemes [14].

The coolant flow for the ERAD is selected to be laminar as the Reynolds number computed as per the Eq 3.1 lies in the laminar region (i.e. Re < 2300).

$$Re = \frac{uL_c}{\nu} \tag{3.1}$$

Here, Re is the reynolds number, L_c is a characteristic length (m), ν is the is the kinematic viscosity of the fluid (m^2/s) and u is the velocity of the fluid with respect to the object (m/s).

The characteristic length L_c, is determined for the internal pipe flow as,

$\frac{R}{L} > 1$, L is the characteristic length

$\frac{R}{L} < 1$, R is the characteristic length

where R is the radius (m) of the pipe and L is the length (m) of the pipe.

Material Data For the full scale ERAD motor simulations where a conjugate heat transfer analysis is conducted, the thermal properties for each parts are given as shown in Table 3.7 and the fluid properties for the air and coolant is given in Table 3.8

Table 3.7: Solid material data for ERAD parts [6]

Solid parts	Density (kg/m^3)	Thermal conductivity (W/mK)	Specific heat (J/kg K)
Frame/housing	2790	168	883
Windings	8933	401	385
Magnets	7500	7.5	410
Shaft	7817	51.9	446
Rubber hoses and seals	1100	0.9	692
Rotor and stator core	7540	31	557
Winding thermal insulation	1350	0.2	1700

For rotor and stator cores, the thermal conductivity is anisotropic due to steel laminations. The thermal conductivity is divided into 31 W/mK as shown in Table 3.7 in the axial direction and 0.5 W/mK in radial direction which is not shown in Table 3.7.

Table 3.8: Fluid material data for ERAD parts [16]

Fluid	Temperature (K)	Density (kg/m^3)	Specific heat (J/kg K)	Thermal conductivity (W/mK)	Dynamic Viscosity (Pa s)
Ethylene Glycol (Coolant)	293.15	1082	3260	0.402	0.00487
	313.15	1069	3340	0.398	0.00257
	333.15	1057	3410	0.394	0.00159
Air	300.15	1.177	1003.62	0.026	0.0000185

3.6 Mesh sensitivity analysis

In finite volume modelling, a finer mesh typically results in a more accurate solution, however at the expense of an increased computation time. We need to have a balance between accuracy and computation time to reach valid results, which must not change abruptly with changes in mesh size. Therefore, a mesh sensitivity analysis is performed to check how much the results deviate with changes in mesh size.

Three different meshes were evaluated for both the simplified and the full ERAD case motor as shown in Table 3.9. The changes in the temperature for the end windings part was studied for all the three cases as shown in Figure 3.10.

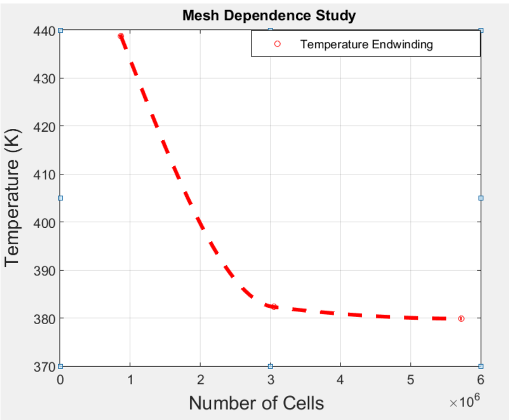

(a) Simplified motor

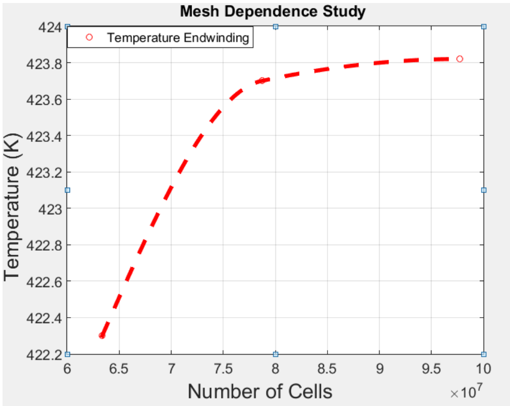

(b) ERAD motor

Figure 3.10: Mesh sensitivity analysis

Here, from the medium mesh size to the finer mesh we see less degree of variations in temperature values for the end windings which is acceptable and therefore, the medium mesh size was chosen as an ideal mesh to save computational efforts and at the same time not compromising on the accuracies of the results.

Table 3.9: Mesh Sensitivity Analysis

Case	Mesh Type	Number of Elements	Temperature of end windings (K)
Simplified motor case	Coarse Mesh	867,563	438.73
	Medium Mesh	3,048,946	382.30
	Finer Mesh	5,729,088	379.87
Full scale ERAD motor	Coarse Mesh	63,368,137	422.30
	Medium Mesh	78,712,167	423.70
	Finer Mesh	97,708,792	423.82

3.7 Wall y^+

It is necessary to determine the appropriate y^+ values when using the near wall modelling approach and to check if all the fluid regions are resolved in the viscous layer. However, as per Eq (2.17), the wall y^+ values are dependent on the frictional velocity as well. Therefore, for the highest working operating point at 12000 RPM, y^+ was checked as in Figures 3.11 and 3.12 for both **simplified motor model** and **full scale ERAD model**. Here, we note that all the regions are in between the wall y^+ range ($0 < y^+ < 5$) in viscous layer region as desired since we can capture the molecular viscosity effects near the wall which play a dominant role in momentum and heat transfer.

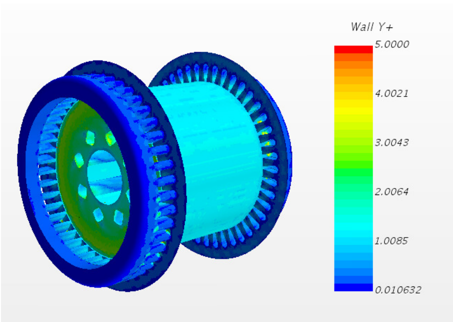

(a) Without end caps and housing.

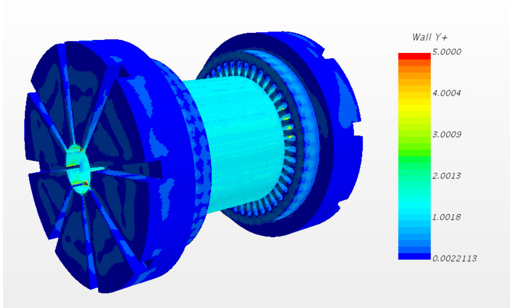

(b) With end caps and housing.

Figure 3.11: Wall y^+ for simplified motor in the internal air region.

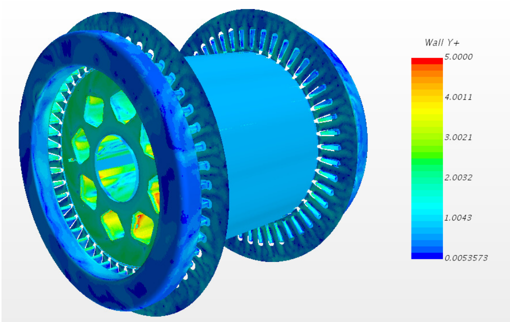

(a) Without end caps and housing.

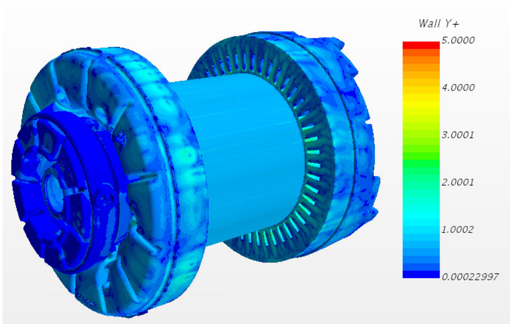

(b) With end caps and housing.

Figure 3.12: Wall y^+ for ERAD motor in the internal air region.

4

Results and Discussions

In this chapter, the results for the simplified motor model, $1/8^{\text{th}}$ section of simplified motor and the full scale ERAD model are presented and discussed. Specifically, the temperature distribution in the internal parts of the electric motor are of great importance to study along with estimations of the heat transfer coefficients for both cases. The numbers presented for each case for temperature and heat transfer coefficients are surface averaged quantities, unless specified otherwise.

4.1 Simplified motor case results

4.1.1 Temperature profiles for internal parts in Simplified motor

Three different steady state simulations were run for three operating points with the losses applied on the surfaces of the internal parts of the electric motor according to Table 3.4. Then, we calculate surface average temperature values for all the internal parts as shown in Table 4.1. Here, the temperature of the end-windings is recorded to be the highest compared to other different parts of the electric motor, which very well matches with the literature due to higher loss values assigned.

A temperature distribution contour is shown in Figure 4.1 for the different parts of the electric motor (the end caps are hidden in these images for clarity) at different operating points when showing the temperature distribution for different parts.

Table 4.1: Steady state temperature for internal parts of simplified motor

Operating points (RPM)	End Caps (K)	End Windings (K)	Housing (K)	Magnets (K)	Rotor Core (K)	Shaft (K)	Stator (K)
4000	326.40	375.98	329.84	320.42	320.53	326.92	332.73
6000	316.54	375.23	321.45	317.75	314.90	316.82	329.88
12000	317.97	362.23	321.51	317.15	321.07	317.10	333.50

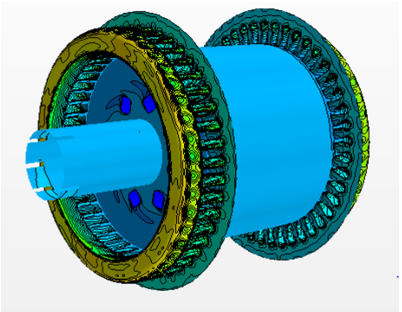

(a) 4000 RPM.

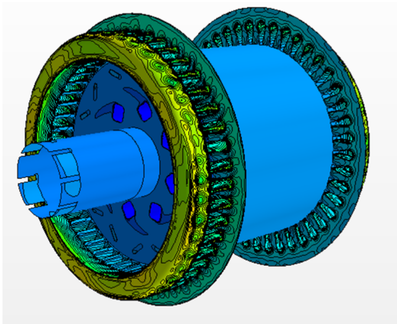

(b) 6000 RPM.

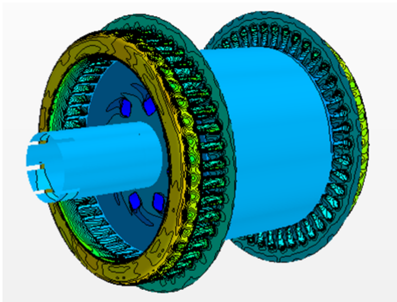

(c) 12000 RPM.

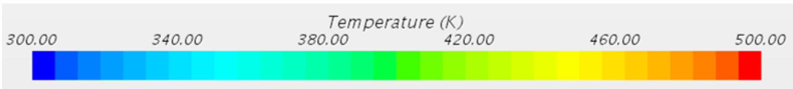

Figure 4.1: Temperature profiles of internal parts at different operating points for simplified motor.

Looking at the air temperature distribution as shown in Figure 4.2, we see that the air around the end-windings has the highest temperature for all the operating points. Also, the air temperature around the rotor holes in the rotor region (thick solid sections in the middle) does not change (i.e. it stays in the ambient conditions). This is expected since conduction in solids is ignored.

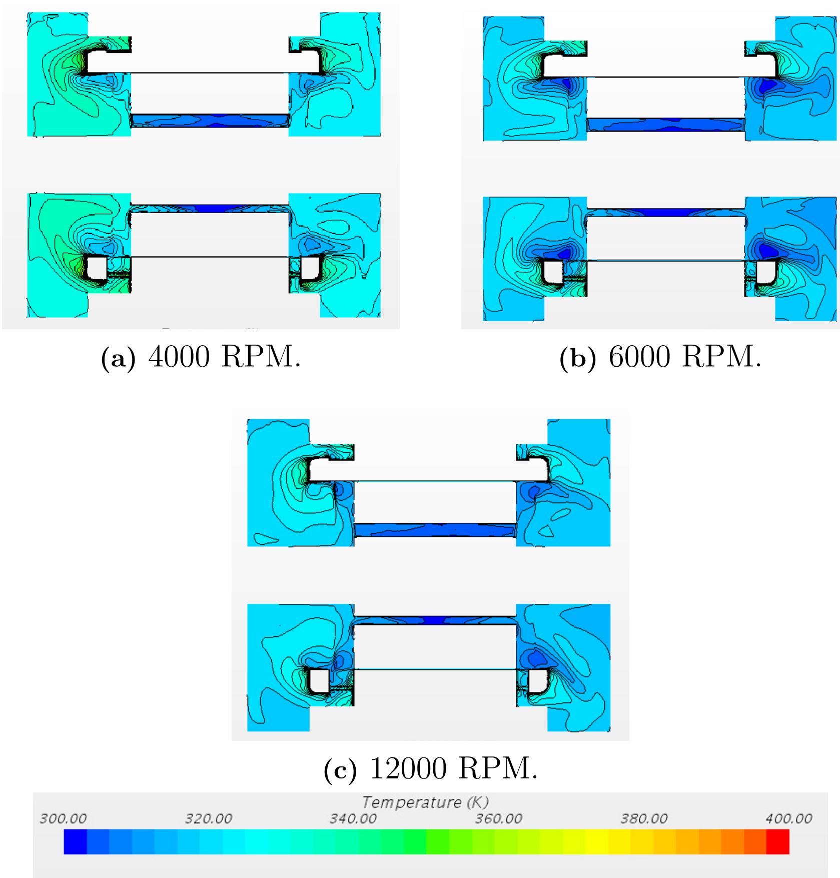

(a) 4000 RPM. **(b)** 6000 RPM. **(c)** 12000 RPM.

Figure 4.2: Air temperature profiles at different operating points for simplified motor.

4.1.2 Convective heat transfer coefficients in simplified motor

The heat transfer coefficients for the heat source parts of the electric motor is computed using the Eq (2.21) from section 2.3.4. Here, the specified y^+ HTC's were used specifying a y^+ value of 30 in the specified y^+ heat transfer coefficient field function of Star CCM+. The following HTC distribution profile is shown in Figure 4.3. Here, the y^+ value of 30 was chosen as a standard practice where one can choose from y^+ value of 30 to 100. In choosing the y^+ values, no matter which values you choose within this range of y^+ you would get different values for the heat tansfer coefficients, but the computed Nusselt number still falls in an acceptable range as per StarCCM+ user manual. In the present work, this couldn't be verified as one has to compute Nusselt numbers for each part and determine characteristic lengths of all those parts which would be a lengthy task to complete, looking at the time frame of the thesis.

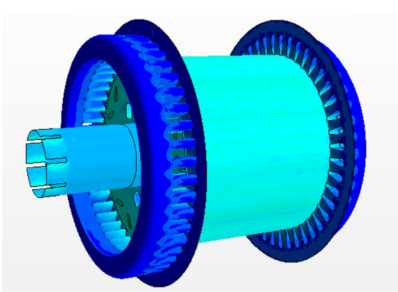

(a) 4000 RPM.

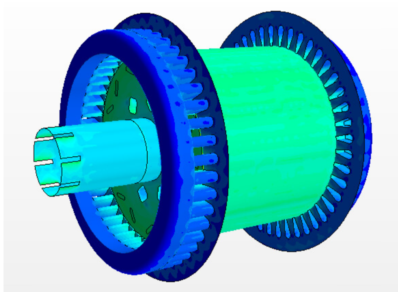

(b) 6000 RPM.

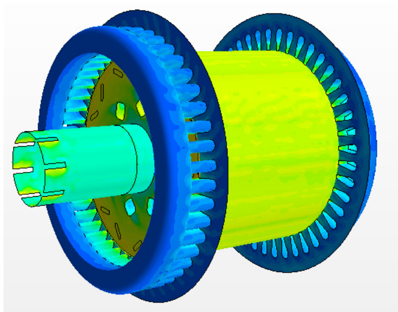

(c) 12000 RPM.

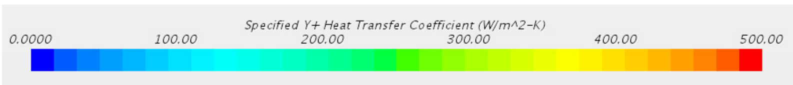

Figure 4.3: Convective heat transfer coefficients at different operating points for simplified motor.

Then, we calculate surface average HTC values for all the internal parts as shown in Table 4.2.

Table 4.2: HTC's for different internal parts of simplified motor

Operating points	**End windings** W/m^{2}K	**Magnets front surface** W/m^{2}K	**Rotor diameter surface** W/m^{2}K	**Rotor front surface** W/m^{2}K	**Stator front surface** W/m^{2}K
4000	20.73	157.30	141.42	137.86	104.25
6000	30.25	219.04	198.87	191.57	146.06
12000	54.67	344.89	332.81	312.08	264.60

Next, the variation of obtained heat transfer coefficients with operating points is as shown in Figure 4.4.

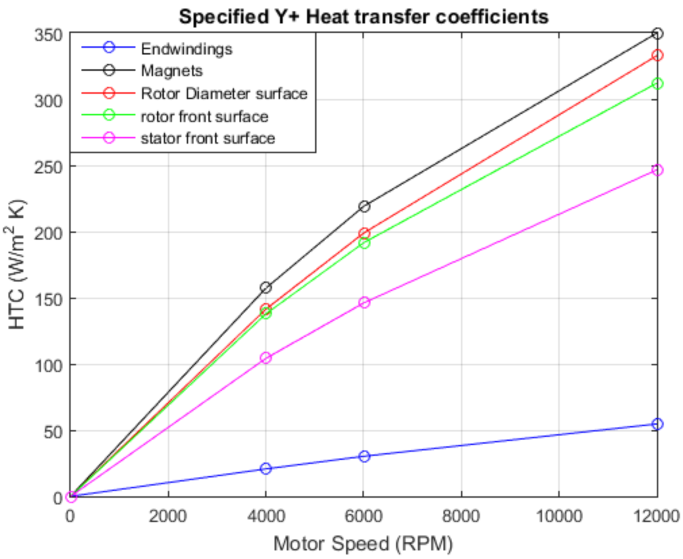

Figure 4.4: Convection heat transfer coefficients vs operating points

Here, we see that the HTC's for different parts of the electric motor increase with increasing motor speed and this is due to higher velocities and mass flow rates of the internal air.
To avoid erroneous assumption of surface heat flows for the ERAD motor since we had total volume losses, we started to perform a conjugate heat transfer analysis for the detailed ERAD motor, for which the results will be shown in the coming sections so that we can apply total losses and investigate complete thermal phenomena.

4.2 $1/8^{th}$ section of simplified motor

Initially, this case was set up to compare the results with that of the simplified case but that could not be possible as the number of stator slots modelled in the simplified case were 46 which made it unsymmetrical. Therefore, in this case we had to remodel the number of stator slots to 48 to attain symmetry which resulted in decrease in surface area for the stator, increase in the surface area of the end windings and change in the position of the slots. However, here we can still compare the results with simplified case to verify that the temperature and heat transfer coefficients quantities are geometry dependent.

A simulation was run for a single operating point (4000 RPM) with the reduced losses to 1/8 of the total losses that was given for the simplified case from Table 3.4.

4.2.1 Temperature profile of $1/8^{th}$ section motor

In this case a similar trend compared to the simplified case was seen where the temperature of the end windings were the highest and the air around the end windings were the hottest with the rotor holes temperature at initial conditions (300 K) as shown in the Figure 4.5.

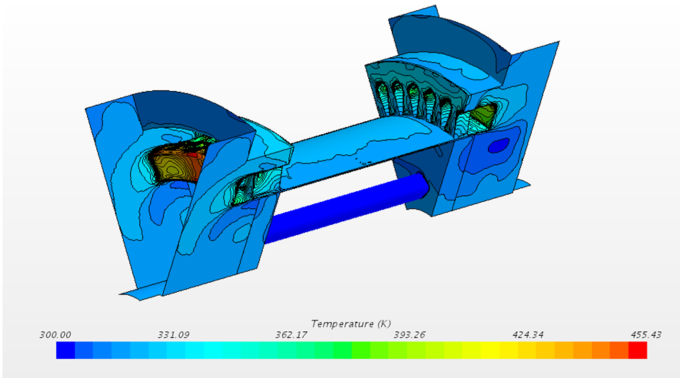

(a) Temperature profile for internal parts.

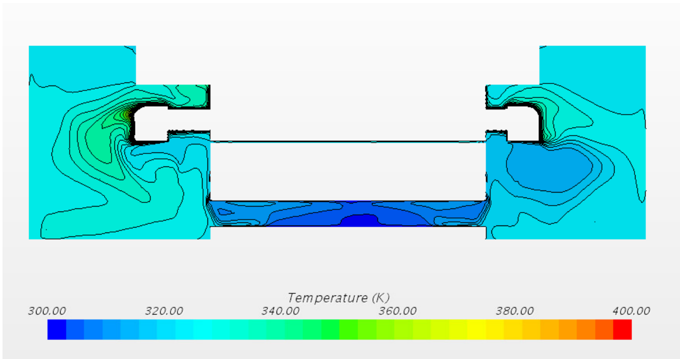

(b) Air temperature profile .

Figure 4.5: Temperature distribution for $1/8^{th}$ section motor model at 4000 RPM.

The surface average temperatures are tabulated for different parts for this case as shown in Table 4.3

Table 4.3: Temperature for internal parts of $1/8^{th}$ section motor

Operating points (RPM)	End Caps (K)	End Windings (K)	Housing (K)	Magnets (K)	Rotor Core (K)	Shaft (K)	Stator (K)
4000	316.05	369.64	319.18	313.43	313.08	315.74	324.92

4.2.2 Convective heat transfer coefficients of 1/8$^{\text{th}}$ section motor

The heat transfer coefficient is computed similarly to the simplified motor case with the y^+ value of 30 and its distribution is as shown in Figure 4.6. The symmetry walls have zero heat transfer coefficients which is shown in the Figure 4.6. This is because these walls act as periodic interfaces where there is no temperature gradients.

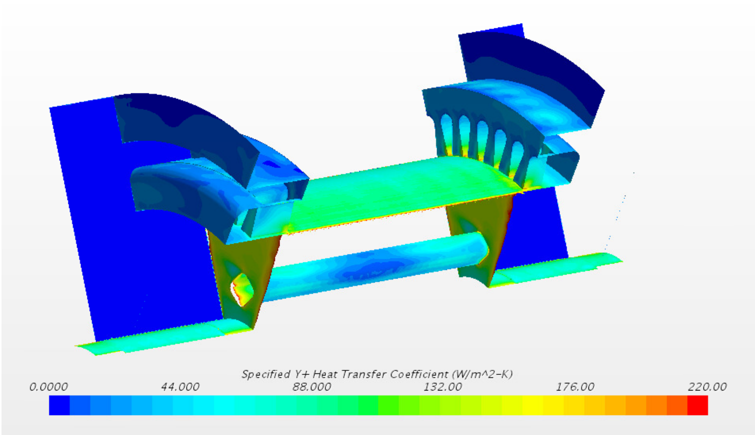

Figure 4.6: Convective heat transfer coefficient at 4000 RPM

The surface average heat transfer coefficient is tabulated as shown in Table 4.4

Table 4.4: HTC's for internal parts of 1/8 $^{\text{th}}$ section motor

Operating points	**End windings** W/m^{2}K	**Magnets front surface** W/m^{2}K	**Rotor diameter surface** W/m^{2}K	**Rotor front surface** W/m^{2}K	**Stator front surface** W/m^{2}K
4000	33.21	150.16	166.95	146.89	73.81

The conclusion from this simulation is that one can use this approach instead of modelling the entire full scale model to reduce computational effort significantly. The total solver elapsed time running on 8 cores for this simulation is 18 hours compared to 54 hours for the full scale model reducing the computation time significantly by 66%.
Also, on comparison of the heat transfer coefficient values with the simplified case as shown in Table 4.2, we see significant differences which is due to change in the geometry as the heat transfer coefficient values are also dependent on the surface area of the geometry.

4.3 Full scale ERAD motor model

A conjugate heat transfer analysis was done on the full scale ERAD model. Similarly, to the simplified case results, the temperature profiles and the dependency of heat transfer coefficients at different operating points were studied. In addition to this, the effect of coolant flow rate and the inlet coolant temperature on the temperature of the coolant and the heat transfer coefficients are studied and explained.

4.3.1 Energy balance for ERAD

Before running simulations for different operating points and for different areas of studies, an energy balance check was performed. This is mainly to check if the law of conservation of energy is satisfied. This check was done for the case of 4000 RPM by plotting the total losses (1630.32 W) that was given as input to different internal parts of the electric motor (green) and the total heat transfer to the coolant (blue) along with the net energy change (red) as shown in Figure 4.7.

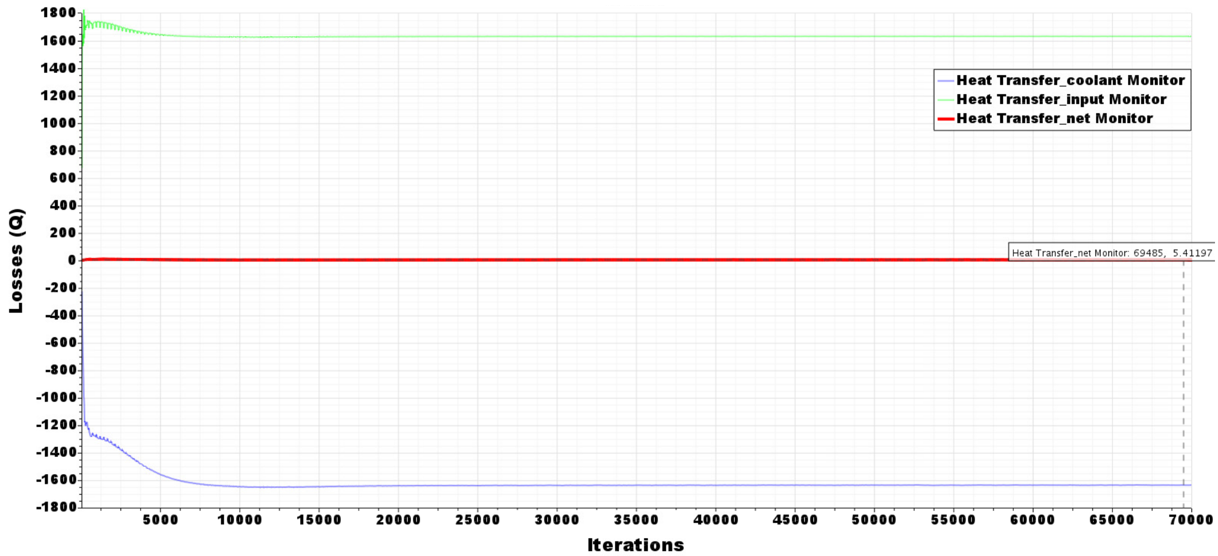

Figure 4.7: Energy balance plot at 4000 RPM

From the Figure 4.7, we see that the net energy change is not in absolute zero, there is a difference of 5.4 W from the input losses to the coolant which is less than 1% error recorded which is acceptable and can be contributed due to numerical errors in the simulations. The difference in the net energy change for different motor speed can be seen in Table 4.5, here we see that as we move at higher speeds, we have higher differences.

Table 4.5: Energy balance at different operating points

Operating point (RPM)	Input losses (P_{total}) (W)	Coolant losses (P_{cool}) (W)	Percentage Error (%)
1000	1324.98	1319.72	-0.39
4000	1630.32	1635.08	-0.29
8000	3125.62	3152.69	-0.86
12000	4359.26	4442.97	-1.92

4.3.2 Temperature profile for internal parts of the full scale ERAD model

Four different steady state simulations were run at four different operating points with the volumetric losses applied in the internal parts of the electric motor as mentioned in Table 3.5.

The surface average temperature values are shown in Table 4.6. Similarly to the simplified case, the temperature of the end windings is the highest compared to other parts of the electric motor, due to higher losses followed by the stator windings.

Table 4.6: Steady state temperature for internal parts of Full ERAD motor

Internal Parts	Temperature (K) at operating points			
	1000 RPM	4000 RPM	8000 RPM	12000 RPM
End windings	371.99	372.67	422.37	456.64
Housing	322.40	324.83	336.23	346.36
Endcaps	328.39	335.37	360.15	383.08
Magnets	339.09	347.13	381.10	410.24
Rotor	338.93	347.00	380.97	410.10
Shaft	336.50	344.62	377.28	405.43
Stator	335.25	338.82	362.12	381.50
Stator windings	361.07	363.21	406.12	436.88

A temperature distribution contour for the internal parts of the electric motor at different operating points is shown in Figure 4.8. Looking at the air temperature profiles in Figure 4.9, we see that the air around the end windings are the hottest compared to the other parts indicating that maximum heat is transferred from this part to the air.

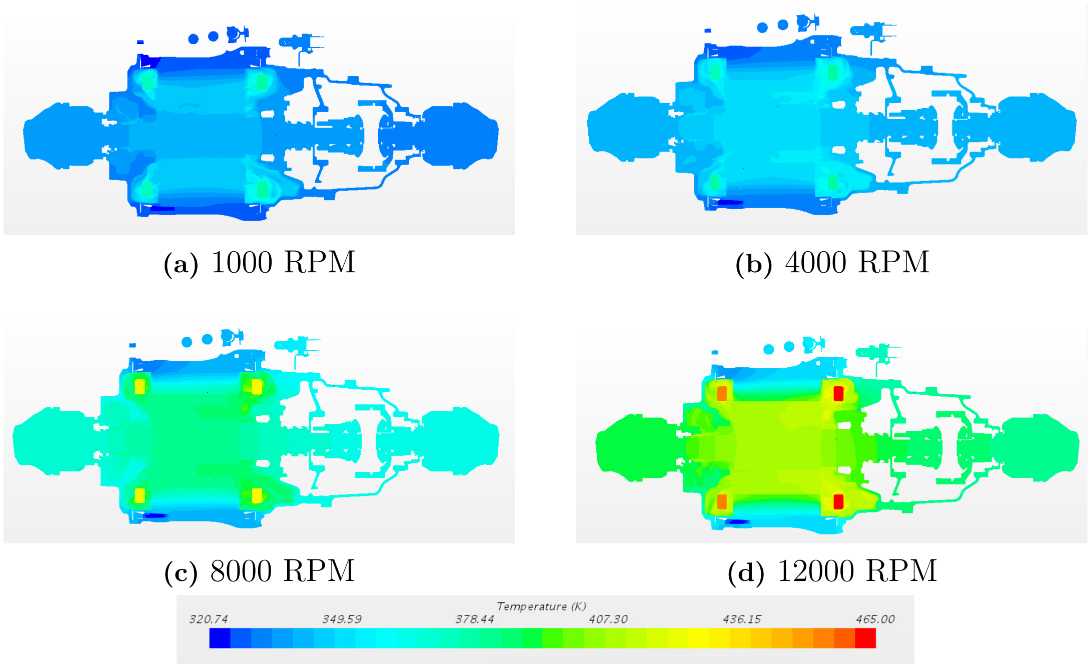

(a) 1000 RPM (b) 4000 RPM

(c) 8000 RPM (d) 12000 RPM

Figure 4.8: Temperature profiles for internal parts at different operating points.

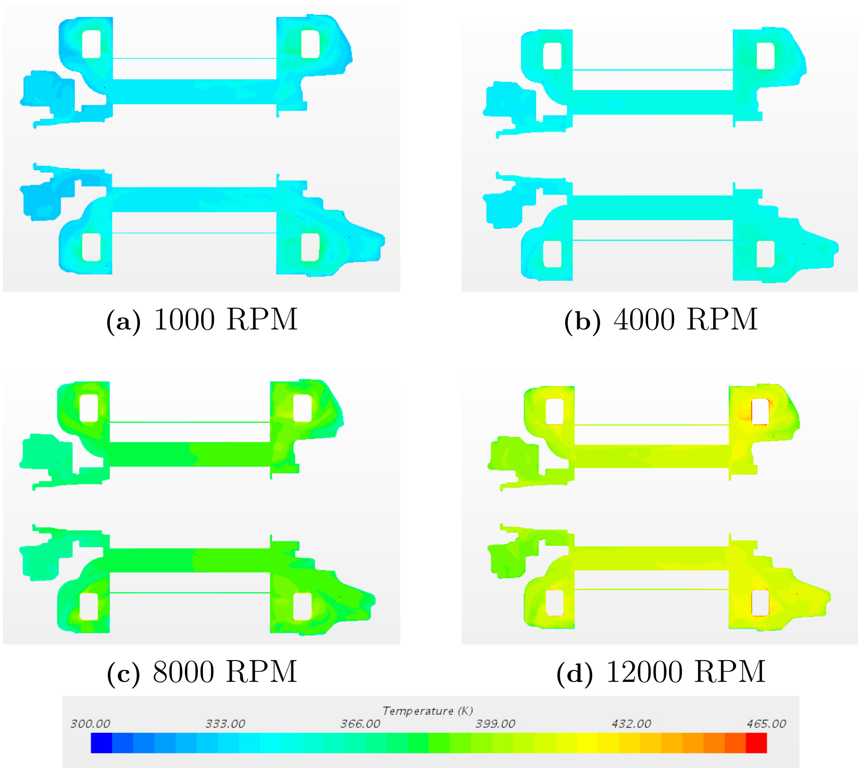

(a) 1000 RPM (b) 4000 RPM

(c) 8000 RPM (d) 12000 RPM

Figure 4.9: Air temperature profiles at different operating points.

The heat transfer values as losses from the surfaces of the internal parts of the motor shown in the Appendix A.4 to the internal air are as shown in Table 4.7

Table 4.7: Heat transfer to internal air at different operating points

Internal surfaces	Losses transferred (W) at Operating points			
	1000 RPM	4000 RPM	8000 RPM	12000 RPM
End caps/housing/ winding thermal insulation	61.42	137.49	367.57	601.24
End windings	-81.42	-163.97	-400.07	-567.27
Rotor diameter surface	4.31	-4.98	-25.06	-49.10
Stator front surface	6.93	28.76	94.40	178.14
Rotor front surface	8.84	10.46	21.25	20.39
Shaft	0.86	1.54	4.12	4.94

In the table, the negative sign represents that the heat is transferred from different surfaces to the air and vice versa for the positive values.

The heat transfer from the surface of the end windings to the air has the highest values at different operating points except at 12000 RPM, but these large numbers become extremely important to study as they dictate the overall temperature inside the motor. The large number for the endcaps/housing/thermal insulation is assumed to be caused by higher air velocities and mass flow rate at the end caps.

Overall the temperature of the motor increases with increasing motor speed due to higher loss values that are given as input.

4.3.3 Convective heat transfer coefficients for the ERAD motor

The heat transfer coefficients for the ERAD case were calculated using the specified y^+ HTC. It has the advantages of being less sensitive to the near wall mesh size and it automatically specifies the fluid reference temperature values that needs to be given as input when calculating the heat transfer coefficients as per (Eq 2.21). Here, y^+ of 30 was chosen as reference again so that it calculates HTC's for the fluid temperature at a y^+ of 30 at different internal parts.

A Specified y^+ HTC contours are shown in the Figure 4.10 and the surface average values are computed for different internal surfaces shown in Table 4.8, 4.9, 4.10 and 4.12 along with their reference fluid temperatures.

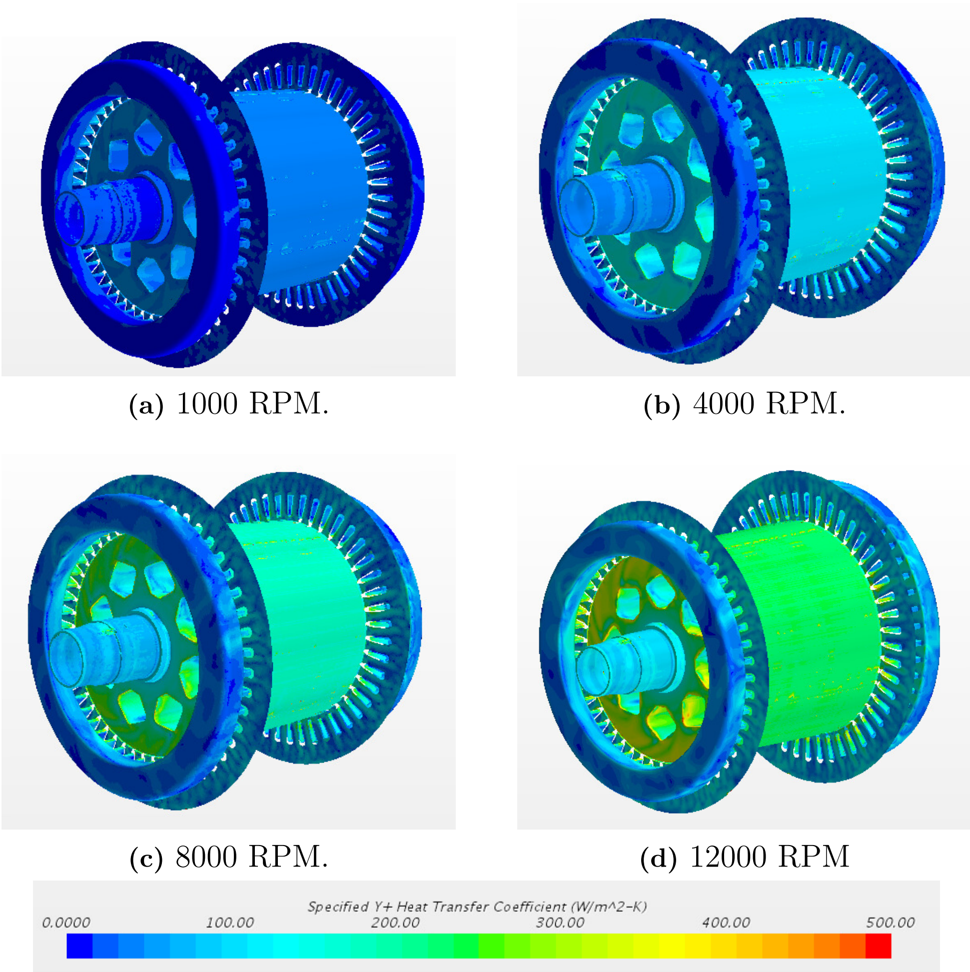

(a) 1000 RPM. **(b)** 4000 RPM. **(c)** 8000 RPM. **(d)** 12000 RPM

Figure 4.10: Convective heat transfer coefficients at different operating points

Table 4.8: Specified y^+ HTC at $y^+ = 30$ for 1000 RPM

Internal surfaces	**Reference fluid temperature (K)**	**Heat transfer coefficient** (W/m^{2}K)
End caps/housing/ thermal insulation	351.70	11.28
End windings	334.37	17.17
Rotor diameter surface	340.94	39.00
Stator front surface	345.35	31.39
Rotor front surface	341.61	28.90
Shaft	338.37	18.86

Table 4.9: Specified y^+ HTC at $y^+ = 30$ for 4000 RPM

Internal surfaces	**Reference fluid temperature (K)**	**Heat transfer coefficient** (W/m^{2}K)
End caps/housing/ thermal insulation	351.87	33.02
End windings	343.83	48.06
Rotor diameter surface	346.34	107.50
Stator front surface	349.33	87.65
Rotor front surface	348.10	88.55
Shaft	345.35	54.33

Table 4.10: Specified y^+ HTC at $y^+ = 30$ for 8000 RPM

Internal surfaces	**Reference fluid temperature (K)**	**Heat transfer coefficient** (W/m^{2}K)
End caps/housing/ thermal insulation	385.95	53.62
End windings	376.34	75.99
Rotor diameter surface	378.57	175.00
Stator front surface	382.21	142.52
Rotor front surface	382.50	144.27
Shaft	378.28	90.49

Table 4.11: Specified y^+ HTC at $y^+ = 30$ for 12000 RPM

Internal surfaces	**Reference fluid temperature (K)**	**Heat transfer coefficient** (W/m^{2}K)
End caps/housing/ thermal insulation	412.91	70.87
End windings	405.47	98.24
Rotor diameter surface	406.44	230.175
Stator front surface	409.47	187.25
Rotor front surface	411.33	187.34
Shaft	405.26	121.44

In specified y^+ HTC we have different fluid temperatures for each parts. One other thing to note that is the heat transfer coefficients calculated are for the internal parts shown in Appendix A.4 with thier surface area values.

Here, we conclude that the heat transfer coefficients are very sensitive to the reference fluid temperatures, therefore a great care must be taken when specifying these reference temperatures. An example shown for the end winding part with calculated specified y^+ HTC's values at y^+ of 30 and 100 are compared and shown for different operating speeds.

Table 4.12: Specified y^+ HTC comparison at different y^+ for end winding

Operating point (RPM)	**Specified y^+ HTC at y^+=30** (W/m^{2}K)	**Specified y^+ HTC at y^+=100**(W/m^{2}K)
1000	17.17	15.04
4000	48.06	39.31
8000	75.99	61.32
12000	98.24	78.99

A comparison of the heat transfer coefficients with operating points are studied and from the Figure 4.11 we conclude that they increase with increase in motor speed similar to that of the simplified case.

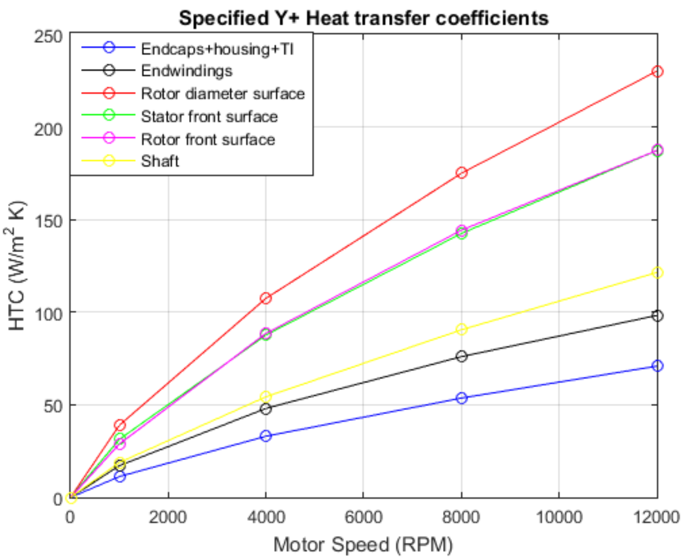

Figure 4.11: Convective heat transfer coefficients vs operating points

4.3.4 Effect of different losses on coolant flow

Here, we will study the dependence of temperature and heat transfer coefficients at a constant flow rate (0.07 kg/s) and inlet coolant temperature (313.15 K) with different losses applied on the internal parts of the motor, as shown in Table 4.13 for different operating points.
The temperature distribution along the cooling path for the coolant are as shown in Figure 4.12

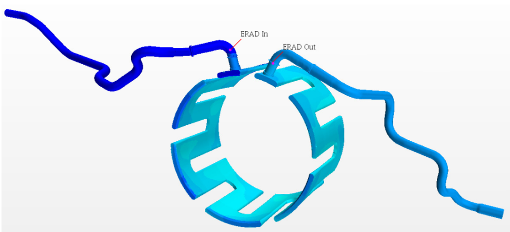

(a) 1000 RPM

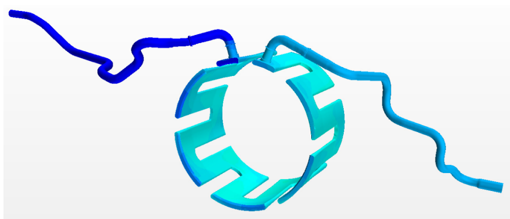

(b) 4000 RPM

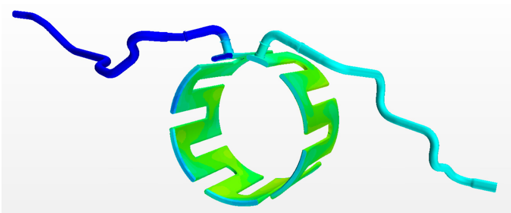

(c) 8000 RPM

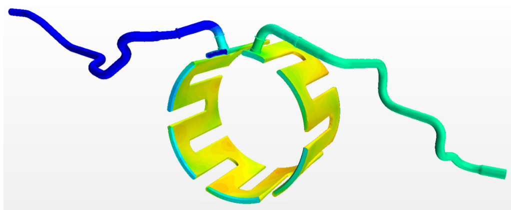

(d) 12000 RPM

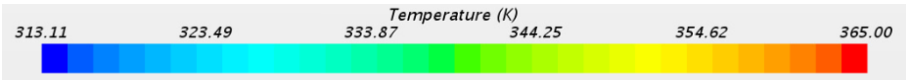

Figure 4.12: Temperature distribution for the coolant at different operating points

The outlet temperatures of the coolant for different operating points are as shown below in the Table 4.13 and these are calculated just after the outlet of the ERAD motor using probe points.

Table 4.13: Outlet coolant temperatures at different operating points

Operating points (RPM)	Outlet coolant Temperature (K)
1000	319.03
4000	320.43
8000	327.34
12000	333.41

The temperature increase of the coolant for a particular loss and flow rate are calculated as in Eqn (4.1) analytically to validate the temperature of the coolant [6].

$$\Delta T_{cool} = \frac{P_{loss}}{\rho_{cool} C_{p,cool} \frac{f_{l/min}}{60\times10^3}} \tag{4.1}$$

where ΔT_{cool} is the temperature increase of the coolant, P_{loss} is heat transfer values, ρ_{cool} is the density of the coolant, $C_{p,cool}$ is the specific heat capacity of the coolant and $f_{l/min}$ is the flow rate of the coolant.

The differences in the temperature increase from the simulation results and analytical results are as shown in Table 4.14. Here, we see a good agreement between the simulation results and the analytical results. The differences between these results are increasing as you increase the operating point which is due to overestimation of the heat transfer which was earlier seen in the energy balance due to numerical errors.

Table 4.14: Coolant temperature increase comparison with analytical calculation

Operating points (RPM)	ΔT_{cool} **Analytical (K)**	ΔT_{cool} **Simulations (K)**	Difference (K)
1000	5.56	5.88	-0.32
4000	6.85	7.28	-0.43
8000	13.13	14.19	-1.06
12000	18.31	20.26	-1.95

Figure 4.13 shows, how the temperature of the coolant varies with increasing losses from different operating points. Here, we see that as we increase the losses the temperature of the coolant increases with motor speed.

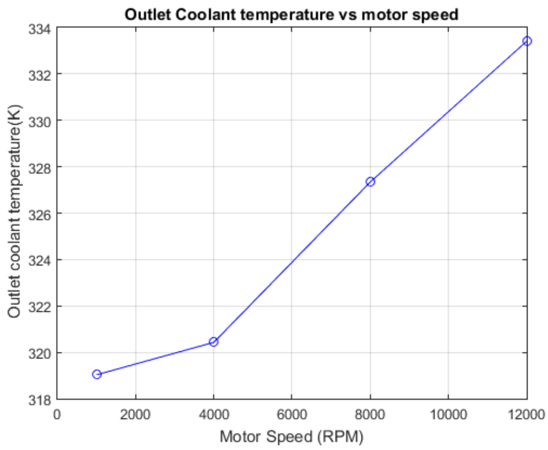

Figure 4.13: Outlet coolant temperature change with motor speed

Next, we investigate how an increase in losses affect the heat transfer coefficients of the coolant flow.

Here, we have computed the heat transfer coefficient specifying the inlet coolant temperature (313.15 K) as the reference fluid temperature. The surface average values are as shown in the Table 4.15 and a heat transfer coefficient contour for the coolant is as shown in the Figure 4.14.

Table 4.15: Convective Heat transfer coefficients for the coolant

Operating points (RPM)	**Heat transfer Coefficients** (W/m^2K)
1000	817.24
4000	817.04
8000	816.16
12000	814.23

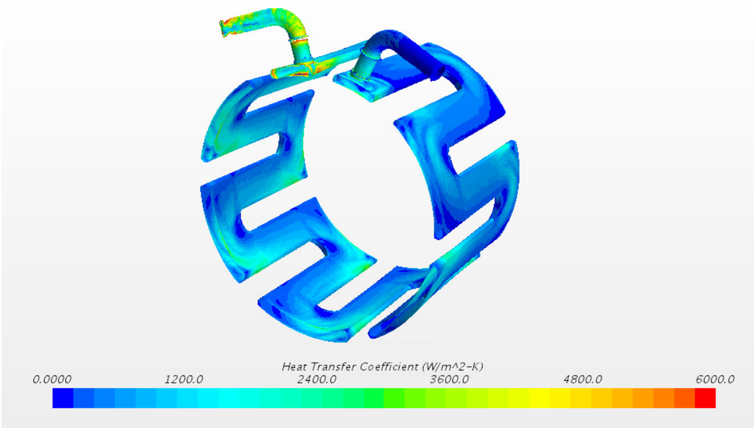

Figure 4.14: Heat transfer coefficient contour for the coolant.

We plot a graph to see how the heat transfer coefficients of the coolant change with the motor speed as shown in the Fig 4.15.

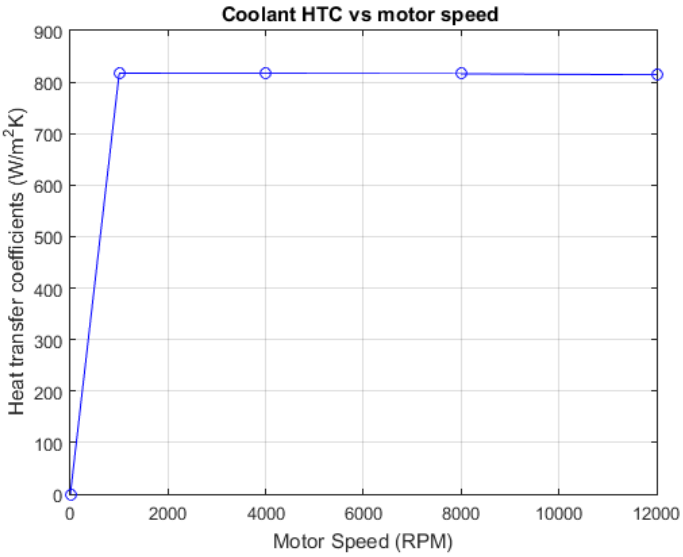

Figure 4.15: Heat transfer coefficient of the coolant with motor speed.

Here, we note that the heat transfer coefficients are constant at different operating points and does not change with increase in losses. The reason for this is because we have a laminar coolant flow for which the HTC's strongly depends on the fluid properties and roughness of the solid surface and not with respect to change in losses.

Therefore, here we can conclude that increase in losses will increase the temperature of the coolant but this do not change the heat transfer coefficients.

4.3.5 Variation of coolant flow rate

Three different flow rates (0.03, 0.07 and 0.1 kg/s) were investigated on the same operating point (8000 RPM) with the same coolant inlet temperature (313.15 K). Here, the thermal properties of the coolant like the density, kinematic viscosity, thermal conductivity and specific heat were kept constant.

The surface average temperatures along with the heat transfer coefficients are as shown in the Table 4.16 and the temperature and heat transfer coefficient contours are as shown in Figure 4.16.

Table 4.16: Temperature and heat transfer coefficients for the coolant at different flow rates

Mass flow inlet (kg/s)	**Outlet coolant temperature (K)**	**Heat transfer Coefficients** (W/m^2K)
0.03 (2 L/min)	344.31	449.99
0.07 (4L/min)	327.34	816.16
0.1 (6L/min)	323.30	1065.47

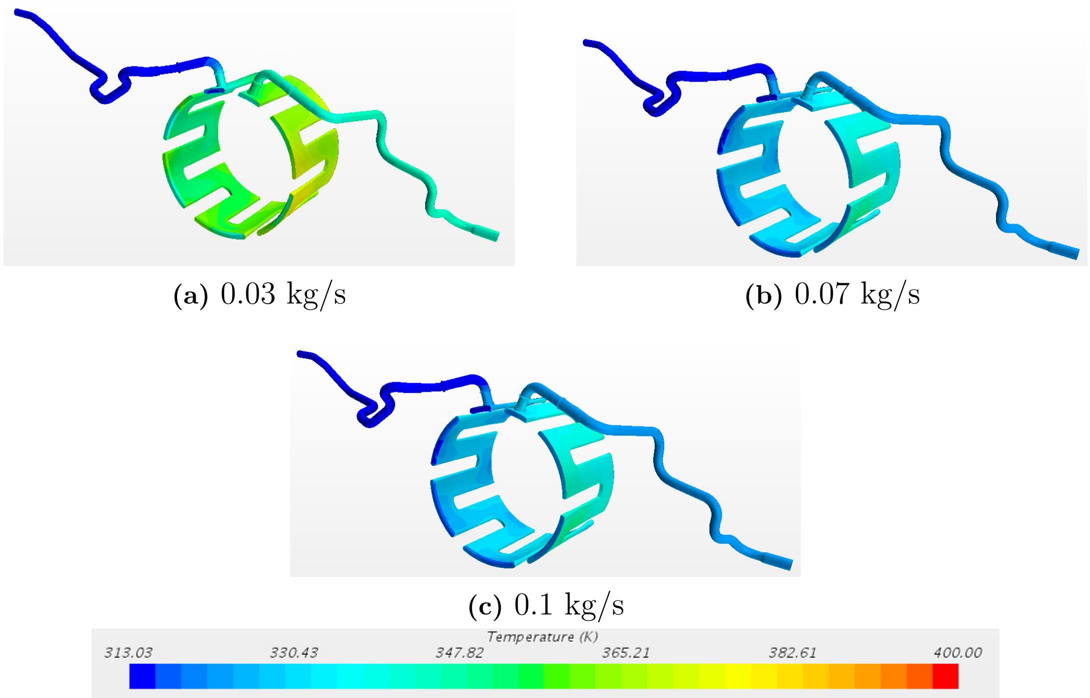

(a) 0.03 kg/s

(b) 0.07 kg/s

(c) 0.1 kg/s

Figure 4.16: Temperature of coolant for different flow rates

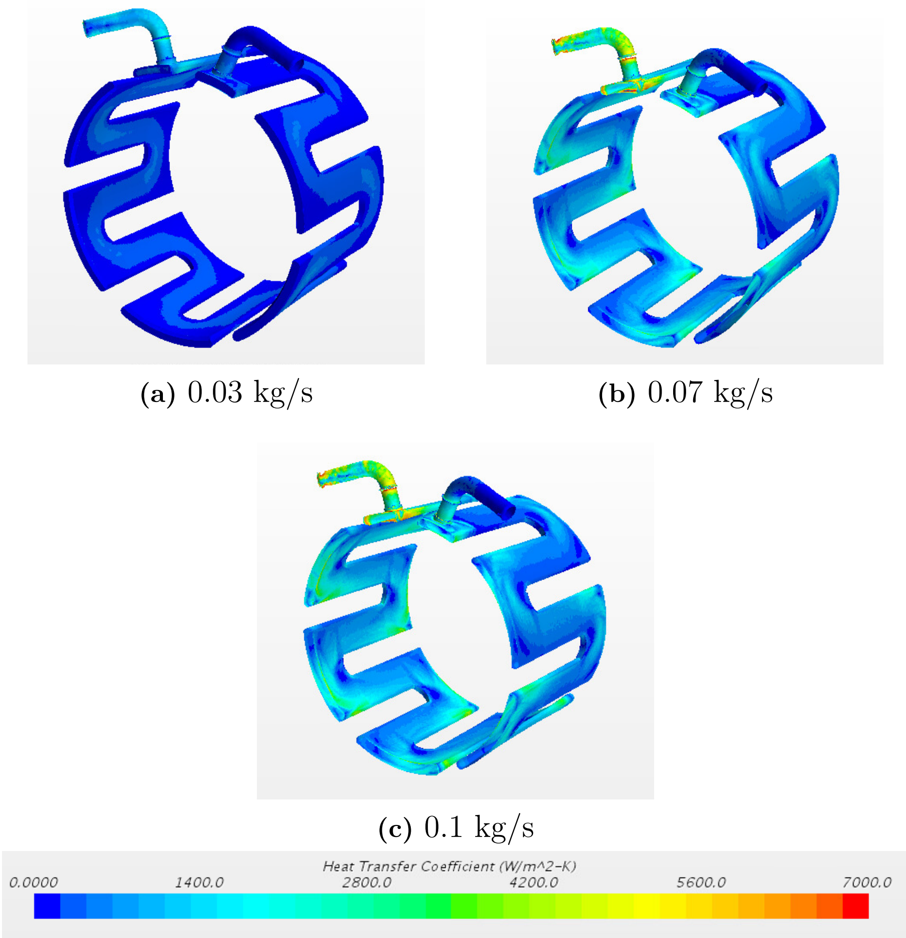

(a) 0.03 kg/s

(b) 0.07 kg/s

(c) 0.1 kg/s

Figure 4.17: Convective heat transfer coefficients of coolant for different flow rates

The temperature change of the coolant with respect to the flow rate is shown in Figure 4.18. With increase of the mass flow rate of the coolant the temperature rise of the coolant decreases.

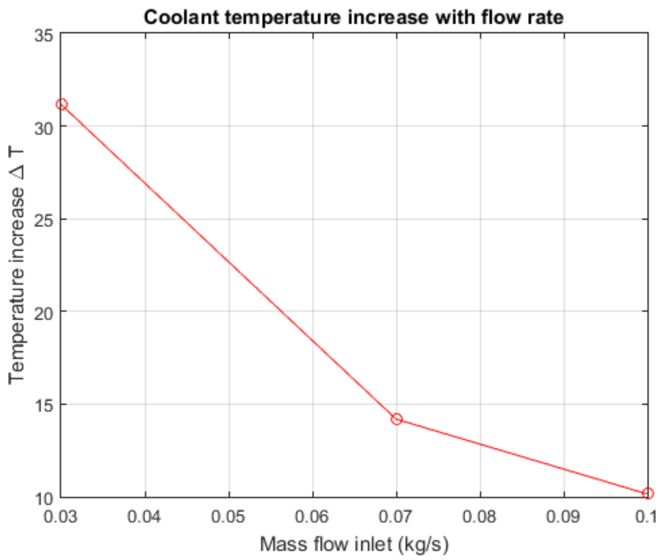

Figure 4.18: Temperature decrease of coolant with flow rate

Now, for the heat transfer coefficients as shown in the Fig 4.19, we see that with increase in the flow rate the heat transfer coefficient values increases linearly.

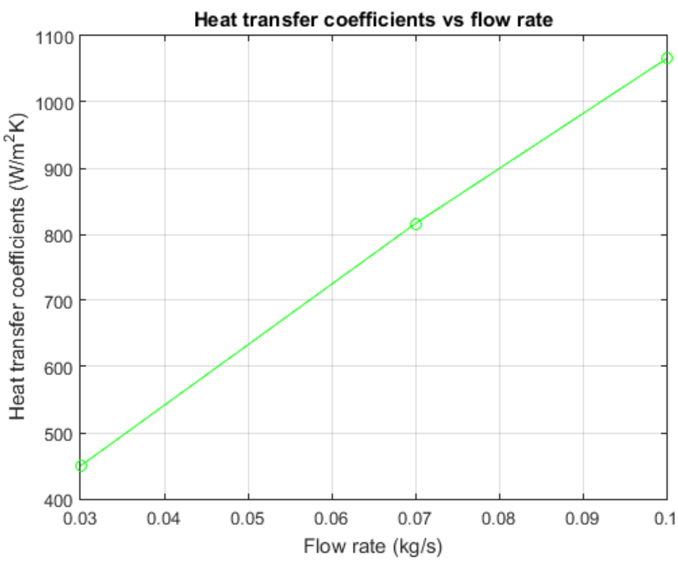

Figure 4.19: HTC increase of coolant with flow rate

4.3.6 Variation coolant inlet temperature

Three different coolant inlet temperatures 293.15 K, 313.15 K and 333.15 K were investigated on the same operating point (8000 RPM) and at a constant flow rate of 0.07 kg/s by changing the coolant thermal properties as per Table 3.8.

The surface average temperatures along with the heat transfer coefficients are as shown in the Table 4.17

Table 4.17: Temperature and heat transfer coefficients for the coolant at different flow rates

Inlet Coolant temperature (K)	**Outlet Coolant temperature (K)**	**Heat transfer Coefficients** (W/m^2K)
293.15	307.86	637.97
313.15	327.34	816.16
333.15	346.86	925.62

Next, we plot a graph for the influence of inlet coolant temperature on the change in outlet coolant temperature as shown in the Fig 4.20. Here although from the Table 4.17 we see increasing temperature values but the difference from the inlet temperature to the outlet is decreasing, i.e., the temperature increase of the coolant decreases and this is due to change in thermal properties of the coolant as per Table 3.8.

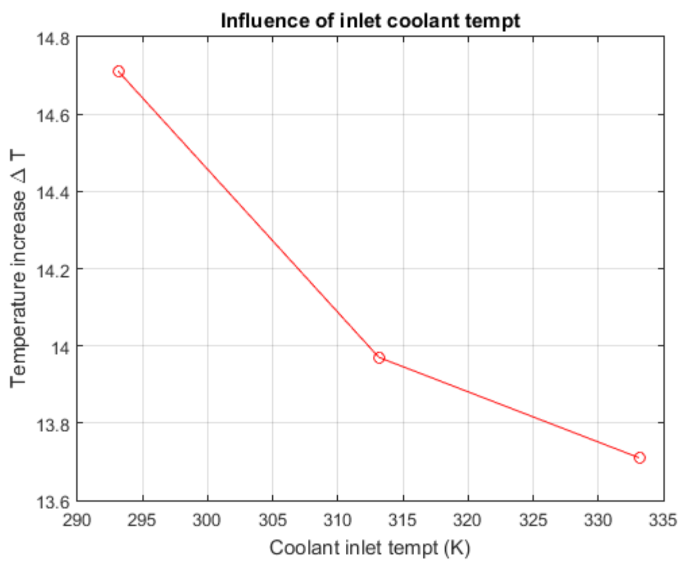

Figure 4.20: Temperature decrease of coolant with inlet coolant temperature

Plotting the heat transfer coefficients as shown in the Figure 4.21, we see an increase in the heat transfer coefficients with increase in inlet temperature of the coolant and this is due change in the reference fluid temperature of the coolant.

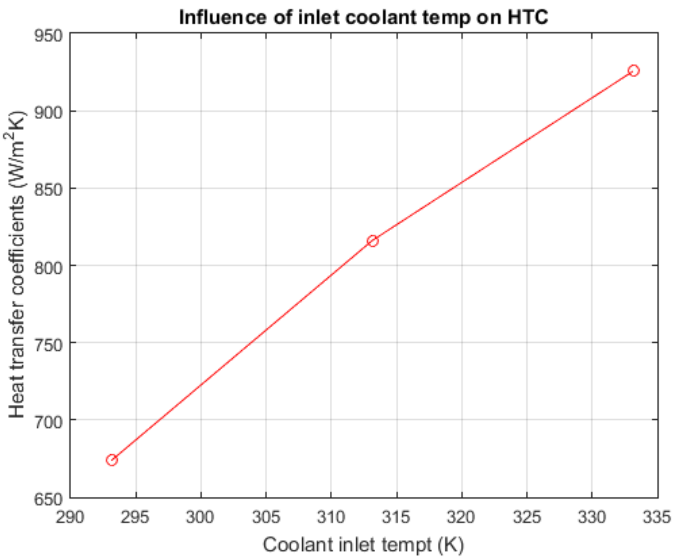

Figure 4.21: HTC increase of coolant with inlet coolant temperature

4.4 Comparison with Lumped Parameter thermal Network models

The simulated volumetric average temperatures from the simulations for an operating point of 8000 RPM of different internal parts of the motor were compared with the results of the preliminary lumped parameter thermal network model (see Appendix A.5) as shown in Table 4.18

Table 4.18: Comparison of CFD results with LPTN

PARTS	**Temperature** $(\deg C)$ **from LPTN**	**Temperature** $(\deg C)$ **from CFD Simulations**	**Difference** $(\deg C)$
End windings	146.00	150.51	-4.51
Housing	67.68	64.51	3.17
Magnets	93.75	107.91	-14.16
Rotor	93.68	107.72	-14.04
Stator	83.47	82.81	0.66
Stator windings	106.31	132.80	-26.49
Air	90.74	101.85	-11.11

Here, we see a large difference for the stator windings part. One reason could be the modelling of winding impregantion and slot liners in our CFD simulations which was simplified.

There is higher temperature differences (higher than +/- 5 degC) for the internal parts at rotor and magnets for which the cause is unknown and future work needs to be carried out to identify the causes. One reason could be is that the LPTN models are generally based on the empirical expressions, whereas the CFD results are based partial differential equations, which makes them more precise. The goal is to use the results from CFD when updating the LPTN network.

5
Conclusions and future work

This thesis work represents a three dimensional steady state thermal analysis of an electric motor using CFD and the following conclusions can be drawn from this thesis work.

1. The obtained heat transfer coefficients from the simplified model and the $1/8^{\text{th}}$ section of the motor model are for comparison only, whereas the heat transfer coefficients obtained for ERAD will be implemented in LPTN.
2. The obtained convective heat transfer coefficients are very sensitive to the chosen reference fluid temperature.
3. The obtained convection heat transfer coefficients increase with increasing motor speed.
4. The specified y^+ HTC is most suitable since it is not first cell height dependent and very suitable for internal flows.
5. The heat transfer coefficients for the laminar coolant flow vary only with fluid and thermal properties including the flow rate.
6. The estimated heat transfer coefficients needs verification either from experiments or from different analytical methods to decide on the right determination of the reference fluid temperatures needed to calculate the HTC values.

5.1 Future work

The future work on this thesis topic is suggested to focus on the following aspects.

1. The geometry of the end windings can be further improved regarding level of detail to enhance quality.
2. Unsteady simulations should be performed in order to predict for changes in the temperature profile for various internal parts of the motor much more accurately.
3. Try to incorporate the Reynolds stress turbulence model in the simulations as it is better with high rotating flows such as an electric motor and the terms are solved directly in RANS equations but here it comes at a price of high computational cost.
4. Estimate the temperature and heat transfer coefficients for a turbulent coolant flow and check how it is affected with different flow and thermal properties.
5. Incorporate the surface roughness details for different parts of the electric motor and compare how the solutions vary implementing this.

Bibliography

[1] WANG Shuwang, ZHANG Yong, HU Junming, Thermal Analysis of Water-Cooled Permanent Magnet Synchronous Motor for Electric Vehicles, 2014 Trans Tech Publications, Switzerland

[2] R-J.Wang, G.C.Heyns., Thermal analysis of a water-cooled interior permanent magnet traction machine //Proceedings of IEEE International Conference on Industrial Technology, Cape Town, 2013:416-421

[3] Y.K Chin, D.A.Staton, Transient thermal analysis using both lumped circuit approach and finite element method of a permanent magnet traction motor //Proceedings of 7th AFRICON Conference, Africa, 2004:1027-1035

[4] Volvo car corporation URL:https://www.media.volvocars.com/global/en-gb/media/photos/188278/drive-e-electric-rear-axle-drive-erad (visited on 14 june 2018)

[5] Yunus A Cengel, Sanford Klein, and William Beckman, Heat Transfer: A practical approach, volume 2nd Edition. McGraw-Hill New York, 1998.

[6] Emma A Grunditz, Design and Assessment of Battery Electric Vehicle Powertrain, with Respect to Performance, Energy Consumption and Electric Motor Thermal Capability, 2016 Chalmers Bibliotek, Reproservice.

[7] Georgios D. Demetriades, Hector Zelaya de la Parra, Erik Andersson and Hakan Olsson, A Real-Time Thermal Model of a Permanent-Magnet Synchronous Motor, IEEE transactions on power electronics, vol. 25, no. 2, february 2010

[8] Chargedevs magazine URL:https://chargedevs.com/features/teslas-top-motor-engineer-talks-about-designing-a-permanent-magnet-machine-for-model-3/ (visited on 14 june 2018)

[9] David A. Staton and Andrea Cavagnino, Convection Heat Transfer and FlowCalculations Suitable for Electric Machines Thermal Models'. In:IEEE Xplore(OCTOBER 2008).

[10] Bin Zhang and Yu Chen, Thermal Model of Totally Enclosed Water-CooledPermanent Magnet Synchronous Machines for Electric Vehicle Applications.In:IEEE Xplore(November 2014).

[11] ldo Boglietti and David Stanton, Evolution and Modern Approaches forThermal Analysis of Electrical Machines. In:IEEE Xplore(March 2009).

[12] Mellor, P. H.; Roberts, D.; Turner, D. R, Lumped parameter thermal-model for electrical machines of TEFC design. // IEE Proceedings-B Electric Power Applications. 138, (1991), pp. 205-218

[13] John D. Anderson, Computational fluid dynamics (the basics with applications).

[14] ANSYS Manual URL:https://www.sharcnet.ca/Software/Ansys/16.2.3/en-us/help/fluth/fluthsecturbnearwalloverview.html (visited on 14 june 2018)

[15] Semantic scholar URL:https://pdfs.semanticscholar.org/51ae/90047ab44f53849196878bfec4232b291d1c.pdf (visited on 30 july 2018)

[16] CERN URL:https://detector-cooling.web.cern.ch/detector-cooling/data/Table 208-3-1.htm (visited on 30 july 2018)

[17] A. Boglietti and A. Cavagnino, Analysis of the Endwinding Cooling Effects in TEFC Induction Motors. In:IEEE Xplore(june 2006).

[18] Engineering pumps URL:http://empoweringpumps.com/ac-induction-motors-versus-permanent-magnet-synchronous-motors-fuji/ (visited on 30 july 2018)

A

Appendix 1

A.1 Loss maps for simplified motor

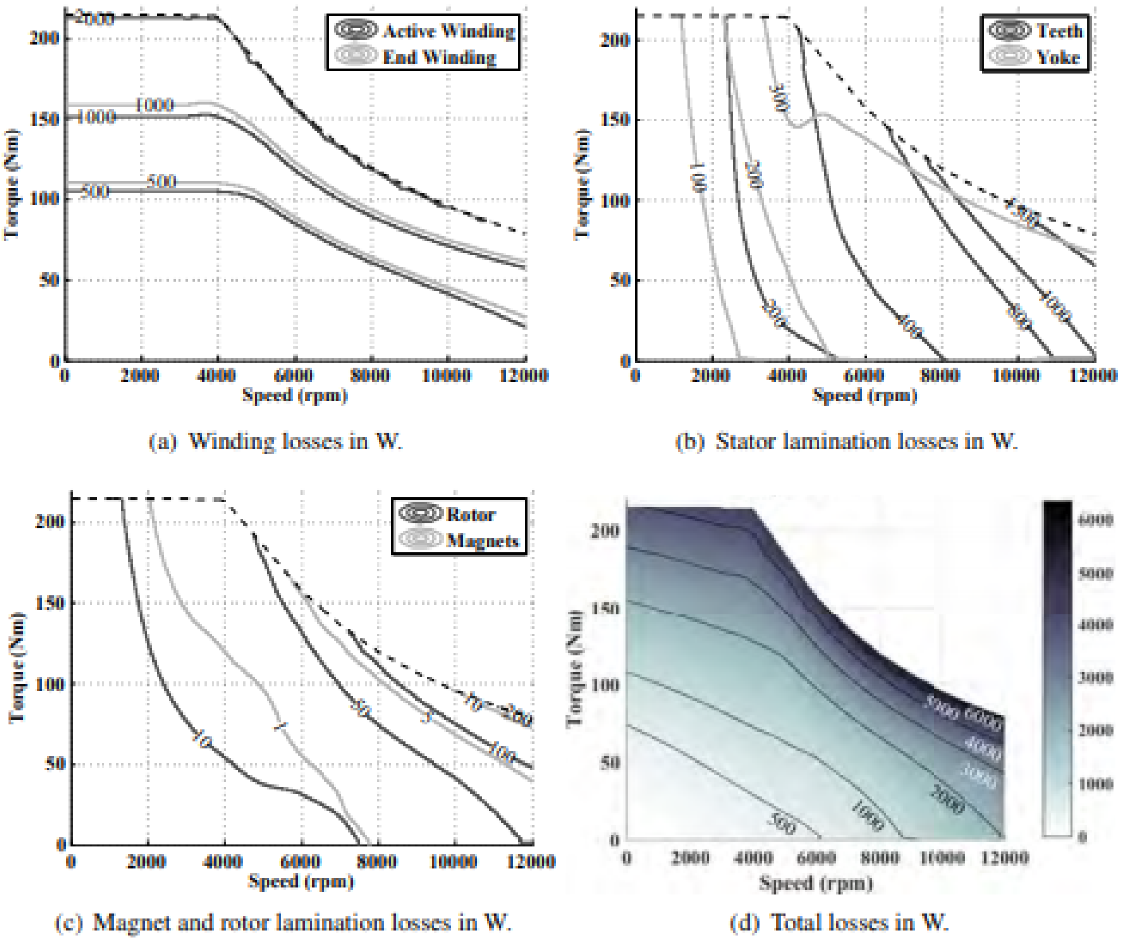

(a) Winding losses in W.

(b) Stator lamination losses in W.

(c) Magnet and rotor lamination losses in W.

(d) Total losses in W.

Figure A.1: Electromagnetic losses as a function of torque and speed, for the HighwayII V-shaped reference motor.[6].

A.2 Loss maps for ERAD motor

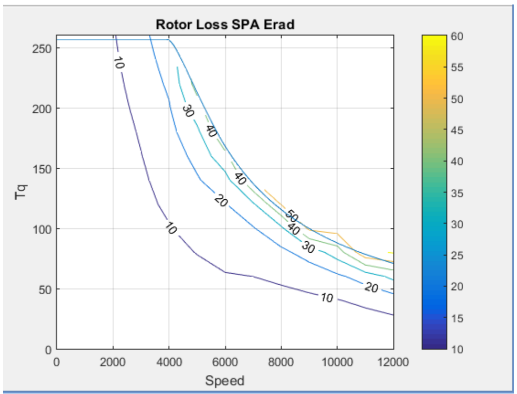

(a) Rotor loss

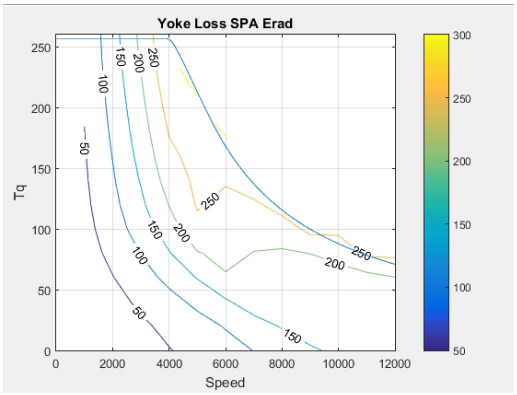

(b) Yoke loss

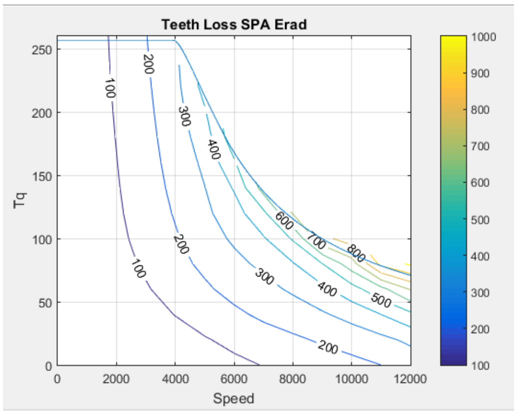

(c) Teeth loss

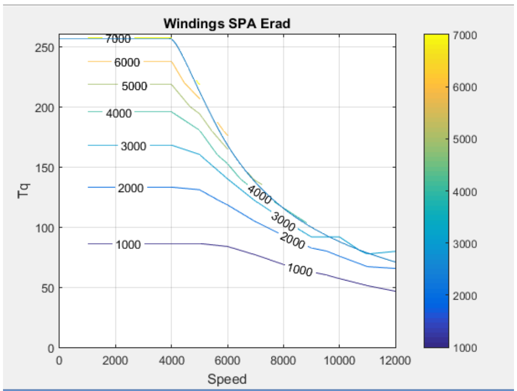

(d) Windings loss

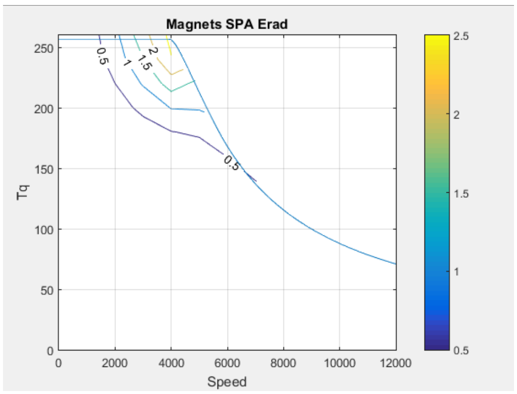

(e) Magnets loss

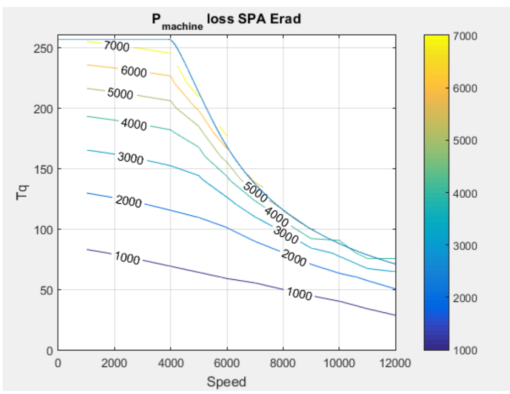

(f) Total losses

Figure A.2: Electromagnetic losses as a function of torque and speed, for the ERAD motor.

A.3 Fluid domains of the internal parts of the simplified motor

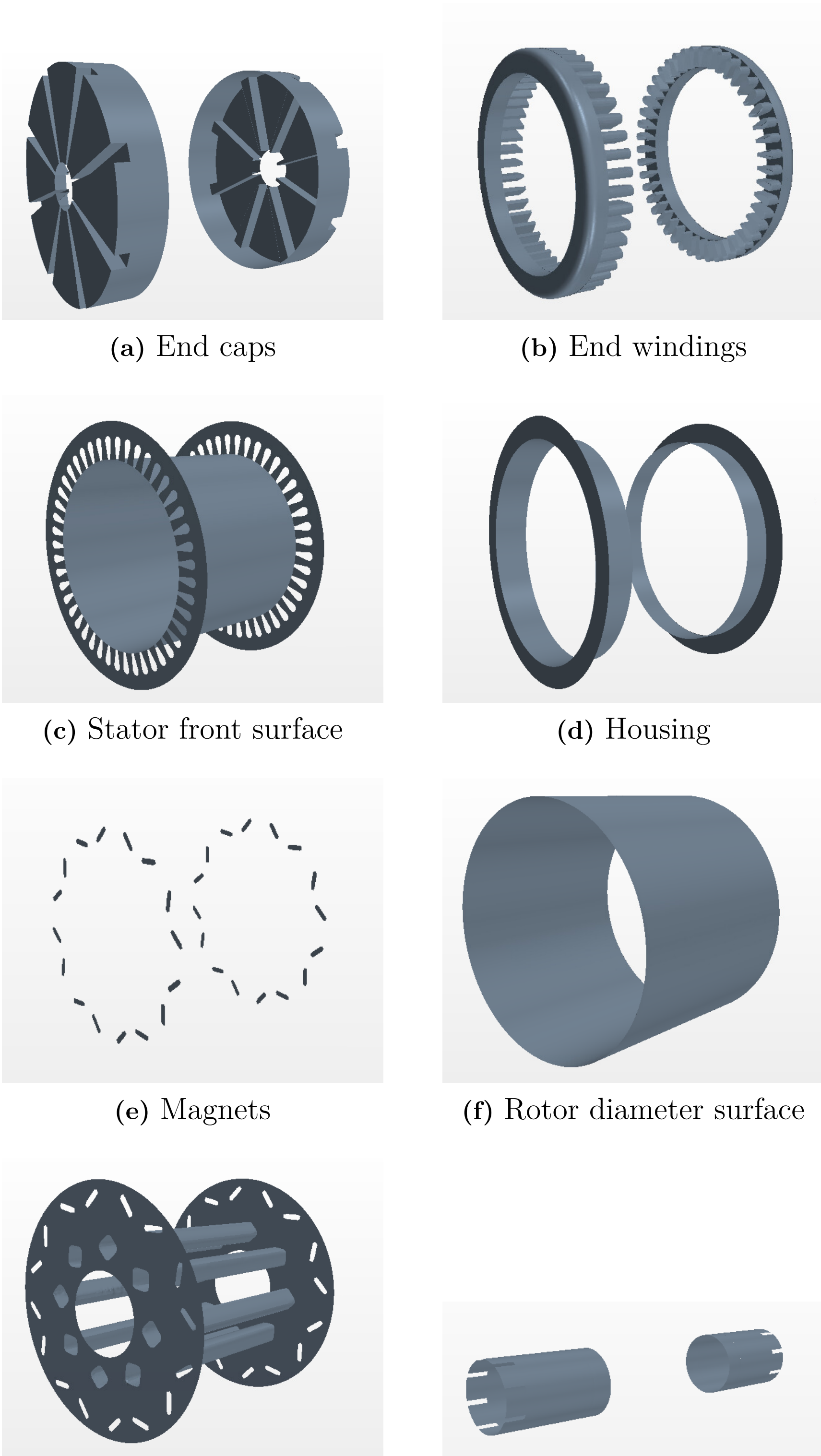

(a) End caps

(b) End windings

(c) Stator front surface

(d) Housing

(e) Magnets

(f) Rotor diameter surface

(g) Rotor front surface

(h) Shaft

Figure A.3: Reduced geometry of the internal parts for the simplified motor

A.4 Areas for the internal surfaces of the ERAD motor

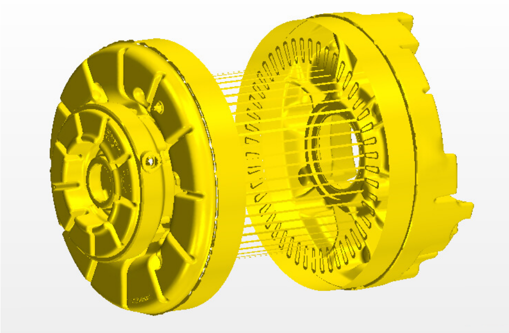

(a) End caps/housing/winding thermal insulation

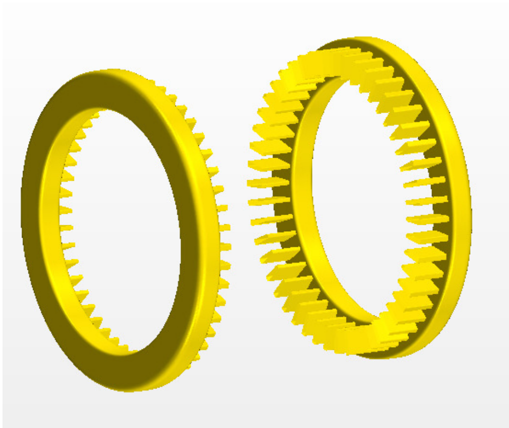

(b) End windings

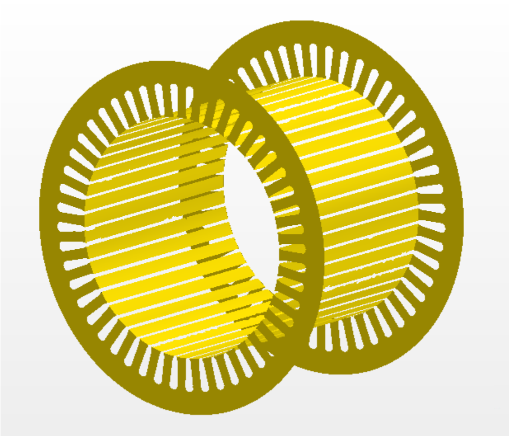

(c) Stator front surface

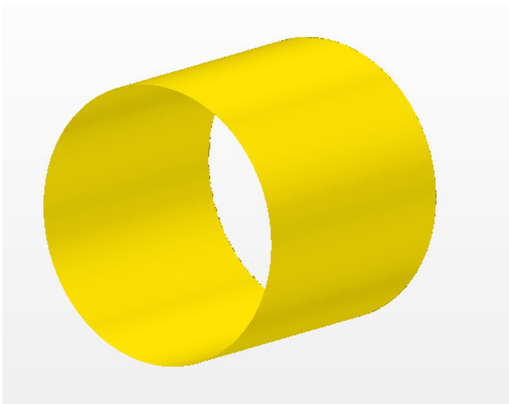

(d) Rotor diameter surface

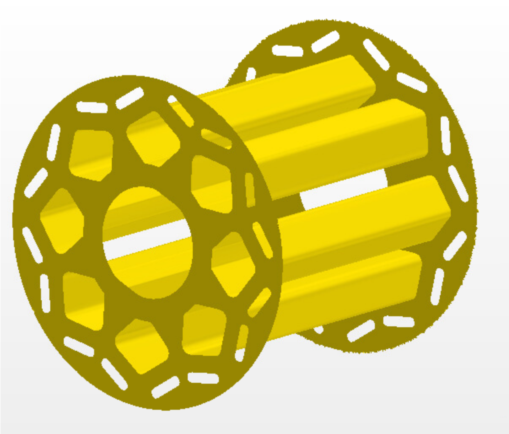

(e) Rotor front surface

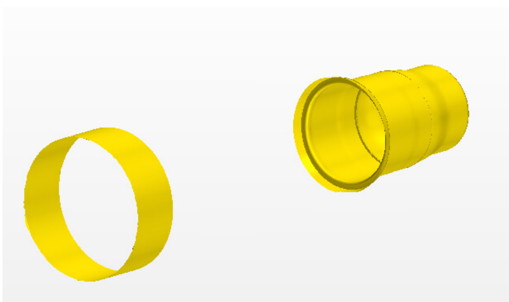

(f) Shaft

Figure A.4: Areas for the internal surfaces of the ERAD motor

Internal parts of ERAD	**Surface area** (m^2)
End caps/housing/winding thermal insulation	0.259
End windings	0.119
Rotor diameter surface	0.060
Rotor front surface	0.103
Stator front surface	0.077
Shaft	0.019

A.5 Lumped Parameter thermal network model for the ERAD motor

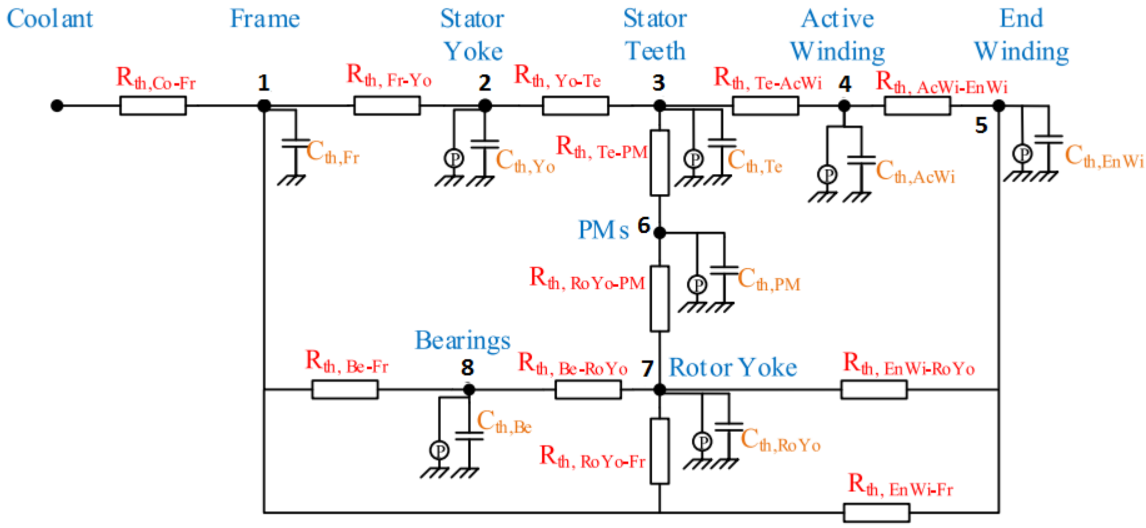

Figure A.5: Lumped Parameter Thermal network model for ERAD